UNITED STATES DEPARTMENT OF THE INTERIOR
GEOLOGICAL SURVEY

Earthquake Hazards in the Pacific Northwest of the Untied States

Compiled by
A. M. Rogers
W. J. Kockelman
G. R. Priest
T. J. Walsh

GROUND ACCELERATIONS FROM SIMULATED M_w=8 CASCADIA EARTHQUAKES

By B. P. Cohee[1], P. G. Somerville, and N. A. Abrahamson

Open-File Report 91-441-N

1991

---

[1]Department of Geophysics, Stanford University, Stanford, CA 94305/Woodward-Clyde Consultants, 566 El Dorado, Pasadena, CA 91101, (818) 449-7650

Foreword

This paper is one of a series dealing with earthquake hazards of the Pacific Northwest, primarily in western Oregon and western Washington. This research represents the efforts of U.S. Geological Survey, university, and industry scientists in response to the Survey initiatives under the National Earthquake Hazards Reduction Program. Subject to Director's approval, these papers will appear collectively as U.S. Geological Survey Professional Paper 1560, tentatively titled "Assessing and Reducing Earthquake Hazards in the Pacific Northwest." The U.S. Geological Survey Open-File series will serve as a preprint for the Professional Paper chapters that the editors and authors believe require early release. A single Open-File will also be published that includes only the abstracts of those papers not included in the pre-release. The papers to be included in the Professional Paper are:

Introduction

Rogers, A.M., Walsh, T.J., Kockelman, W.J., and Priest, G.R., "Assessing and reducing earthquake hazards in the Pacific Northwest: An overview

Tectonic Setting

Paleoseismicity

Adams, John, "Great earthquakes recorded by turbidites off the Oregon-Washington margin"

Atwater, Brian, "Coastal evidence for great earthquakes in western Washington"

Nelson, Alan R. and Personius, Stephen F., "The potential for great earthquakes in Oregon and Washington: An overview of recent coastal geologic studies and their bearing on segmentation of Holocene ruptures, central Cascadia subduction zone"

Peterson, C. D. and Darienzo, M. E., "Discrimination of climatic, oceanic, and tectonic forcing of marsh burial events from Alsea Bay, Oregon, U.S.A."

Tectonics/Geophysics

Goldfinger, C. Kulm, V., Yeats, R., Appelgate, B., MacKay, M., and Cochrane, G., "Active strike slip faulting and folding in the Cascadia plate boundary and forearc, in central and northern Oregon"

Ma, Li, Crosson, Robert, and Ludwin, Ruth, "Focal mechanisms of western Washington earthquakes and their relationship to regional tectonic stress"

Snavely, P. D., Jr., "Cenozoic evolution of the continental margin of Oregon and Washington"

Weaver, C. S. and Shedlock, K. M., "Estimates of seismic source regions from considerations of the earthquake distribution and regional tectonics"

Yeats, Robert, Graven, E.P., Werner, K.S., Goldfinger, C., and Popowski, T, "Tectonic setting of the Willamette Valley, Oregon"

Earthquake Hazards

Ground Motion Prediction

Cohee, B.P., Somerville, P.G., Abrahamson, N.A., "Ground motions from simulated Mw=8 Cascadia earthquakes"

King, Kenneth, Carver, D., Williams, R., Worley, D., "Site response studies in west and south Seattle, Washington"

Madin, Ian P., "Earthquake-hazard geology maps of the Portland metropolitan area, Oregon"

Silva, Walter, Wong, Ivan, and Darragh, Robert, "Engineering characterization of strong ground motions with applications to the Pacific Northwest"

Ground Failure

Chleborad, A. F. and Schuster, R. L., "Earthquake-induced ground failure associated with the April 13, 1949, and April 29, 1963, Puget Sound area, Washington, earthquakes"

Grant, W. P., Perkins, W. J., and Youd, L., "Liquefaction susceptibility maps for Seattle, Washington North and South Quadrangles

Earthquake Risk Assessment

Wang, Leon R.L., Wang, Joyce C.C., and Ishibashi, Isao, "GIS applications in seismic loss estimation model for Portland, Oregon water and sewer systems"

Implementation

Kockelman, William J., "Techniques for reducing earthquake hazards--An introduction"

Booth, Derek B. and Bethel, John, "Approaches for seismic hazard mitigation by local governments--An example from King County, Washington"

May, P.J., "Earthquake risk reduction prospects for the Puget Sound and Portland Areas"

Perkins, J.B. and Moy, K.K., "Liability for earthquake hazards or losses and its impacts on Washington's cities and counties"

Preuss, Jane and Hebenstreit, G. T., "Integrated hazard assessment for a coastal community: Grays Harbor"

Contents

List of Tables

Illustrations

ABSTRACT

The amplitude and duration of strong ground motions from hypothesized M_w=8 subduction zone thrust earthquakes in the Puget Sound - Portland region were estimated using a semi-empirical simulation procedure. The procedure was validated for large subduction zone earthquakes by modeling acceleration time histories and response spectra from the 1985 M_w=8 Michoacan and Valparaiso mainshocks. We found that models of slip distribution on the Michoacan and Valparaiso fault planes derived from the analysis of strong motion and teleseismic velocity seismograms also explain the higher frequency motions of the recorded accelerograms. Quantitative measures of the agreement between the recorded and simulated response spectra were used as estimates of the modeling uncertainty.

Ground motions were simulated for two fault models, representative of the two different subduction geometries beneath the Puget Sound and Portland regions. Identifying the deepest extent of potential rupture on the plate interface is the most critical geometrical source parameter for estimating ground motions in the Puget Sound - Portland region, since this controls the closest approach of the rupture surface. We have used a geometry based on earthquake locations which places the downdip limit of rupture approximately 50 km west of both Seattle and Portland. A geometry in which the plate interface is arched at depths shallower than 40 km beneath western Washington would place the downdip limit directly beneath Puget Sound, and result in much larger ground motion estimates in Puget Sound.

Given the location of the potential rupture surface that we have assumed, the largest cause of uncertainty in estimated ground motions in the Puget Sound - Portland region is due to uncertainty in the distribution of slip (asperities) with depth on the plate interface. As the asperities become deeper, they become closer to the urban regions of the Puget Sound - Portland region, causing the ground motions there to increase. As a result of the increasing depth of the asperity, the attenuation of peak acceleration with distance becomes more gradual. Although the dip of the Oregon fault model is nearly twice that of the western Washington model, the ground motions for the two regions are not very different.

The attenuation of peak acceleration with distance r from the fault asperity is given by

$$\ln(PGA) = 15.5 - 3.33 \ln(r + 128) + 0.79s$$

where s is a site term equal to 0 for rock and 1 for soil. This relation is appropriate for $25<r<175$ km and M_w=8. When distance r is the closest distance to the fault plane, the attenuation relation is

$$\ln(PGA) = 2.8 - 1.26 \ln(r) + 0.79s.$$

This relation should only be used for $30<r<100$ km and M_w=8.

Formal estimates of uncertainty in the calculated ground motions were obtained by considering both parametric uncertainty (estimated from ranges of source models of hypothesized Cascadia subduction earthquakes) and modeling and random uncertainty (estimated from the misfit between recorded and simulated ground motions of the 1985 Michoacan and Valparaiso earthquakes). For periods less than 1 sec, the estimated response spectral velocities on soil sites in the Seattle - Olympia region are about twice those recorded during the 1949 Olympia and 1965 Seattle Wadati-Benioff zone earthquakes, and the durations of strong motion on rock sites are significantly longer (45-60 sec vs. 10-15 sec).

INTRODUCTION

Strong motion simulation procedures play an important role in complementing conventional empirical approaches to the estimation of strong ground motions for seismic hazard analyses. They provide a means of

augmenting the relatively sparse set of strong motion recordings close to large earthquakes, giving more confidence in the estimation of ground motion characteristics for seismic design. This is especially pertinent in regions such as the Pacific Northwest where there is a complete absence of historical subduction thrust earthquakes and hence an absence of recorded strong ground motions. Simulation procedures also provide a means of estimating the dependence of strong ground motions on variations in specific fault parameters; in the empirical data base, these dependencies are difficult to isolate from the many factors that determine strong motion characteristics. The uncertainty in ground motion predictions from the modeling procedure can be quantified by comparisons between recorded and simulated motions and by parametric studies (Abrahamson *et al.*, 1990, 1991), facilitating their use in engineering studies. Simulation procedures also provide a means of including specific information about the earthquake source, the wave propagation path between the source and the site, and local site response in the estimation of ground motions. Time histories can be generated whose wave composition, duration, and frequency content reflect these specific conditions, rather than those contained in the empirical data base. Such time histories are of growing importance as methods for analyzing the non-linear response of structures are developed.

In estimating seismic hazards in Cascadia, it is necessary to consider three earthquake source zones: (*i*) the shallow plate interface: if it has the potential to generate large subduction earthquakes, significant ground motions will occur throughout the region; (*ii*) the intraslab (Wadati-Benioff) zone, the source of the largest earthquakes (1949 M=7.1 Olympia and 1965 M=6.5 Seattle) and the strongest ground motions in the region during this century; and (*iii*) the shallow crustal zone, the likely source of the 1872 M=7.4 north Cascades earthquake. Ground motions from the shallow plate interface (thrust zone) are the subject of this paper.

Although the seismic potential of the Cascadia subduction zone remains uncertain, there exists the possibility that the plate interface may generate great earthquakes (Heaton and Kanamori, 1984; Atwater, 1987; Adams, 1990). Accordingly, we have estimated strong ground motions in the Seattle - Portland region from hypothesized large thrust earthquakes on the Cascadia plate interface. In preparation for applying the ground motion simulation procedure to Cascadia, we modeled strong motion recordings of the 1985 M_w=8 Michoacan, Mexico and Valparaiso, Chile earthquakes, and evaluated the modeling and random uncertainty (Somerville *et al.*, 1991). Ground motion estimates for western Washington and Oregon were then made for M_w=8 earthquakes on the Cascadia plate interface using a range of source parameters. These ground motion estimates are described in detail by Cohee *et al.* (1991). This paper summarizes the most important results of this work, and identifies those aspects of source characterization that most strongly influence the uncertainty of ground motion estimates in Cascadia.

The expected magnitude of a Cascadia subduction earthquake is unknown. Although a typical Cascadia event might be as large as magnitude 9, the lack of strong motion recordings for events of this size precludes quantitative evaluation of the uncertainty in the ground motion of a M_w=9 earthquake. When ground motions for a M_w=8 Cascadia event are understood, the pertinent question of scaling peak accelerations for larger earthquakes may be better addressed. Recent work on scaling of large subduction earthquakes in Mexico is found in Hartzell and Heaton (1988), Day *et al.* (1988), and Singh *et al.* (1989). The ground motion estimates presented here are region-specific, but not site-specific. The objective of this paper is to provide baseline, rock-site response spectra for the study area. Prediction of site-specific response spectra for soil sites would need to consider frequency dependent site response (for example, see King *et al.*, 1990).

The primary reason for selecting the Michoacan and Valparaiso earthquakes was their similarity in subduction zone geometry to that of Cascadia. In both cases, the shallow plate interface dips at a relatively shallow angle, and a substantial part of the fault rupture surface underlies land. This geometry is similar to that in Cascadia and is quite different from that in most other subduction zones, where the fault rupture surface usually has a steeper dip and lies entirely in the offshore region. In addition to their geometrical compatibility with the Cascadia subduction zone, both events were well recorded by a large number of stations at close distances. Also, a good deal is known about their source characteristics, including estimates of the timing and distribution of slip over their fault rupture surfaces. In the simulation procedure, we use these slip distribution models to represent the heterogeneity of the rupture process.

Several different methods for simulating strong ground motions have been tested against recorded strong motions of subduction earthquakes by other investigators. The most common approach has been the empirical Green's function summation method, in which strong motion recordings of smaller earthquakes are summed and lagged to simulate the rupture of a larger event. This method has been applied to the 1983 Nihonkai Chubu

earthquake by Irikura (1986), Kamiyama (1988), and Takemura and Ikeura (1988); the latter authors also studied five other large Japanese subduction earthquakes. In this approach, the empirical Green's functions represent both the source and the wave propagation effects, which is most appropriate if recordings suitable for use as empirical Green's functions are available in the region where the motions of the larger event are to be simulated. Heaton and Hartzell (1989) applied this method to the Cascadia subduction zone using empirical source functions from Japanese subduction earthquakes.

In regions where no strong motion recordings are available for use as empirical Green's functions, it is more appropriate to calculate the Green's functions using a seismic velocity structure model appropriate for the region (Hadley *et al.*, 1982). This approach was used by Day *et al.* (1988) in simulating the strong motion recordings of the 1985 Michoacan earthquake, and estimating strong motions from Cascadia subduction earthquakes. Their source model was composed of a series of cracks represented by theoretical source functions, and the Green's functions were calculated for a layered crustal model using generalized rays.

SIMULATION PROCEDURE AND UNCERTAINTY

There exist several methods for simulating high frequency strong ground motion close to a large fault. Some of these methods have been described briefly in Joyner and Boore (1988). The existing methods can be broadly classified into three categories: (*i*) deterministic methods, (*ii*) stochastic methods, and (*iii*) hybrid methods. The deterministic methods (Aki, 1968; Haskell, 1969) use kinematic source models and require that the distribution of slip on the fault is known. These methods have only been successful at frequencies less than about 3 Hz. On the other hand, the stochastic methods model the earthquake acceleration as random noise in the band between corner frequency and f_{max}, and the spectral shape is given by the Brune spectrum (Hanks and McGuire, 1981). These methods are computationally very efficient but they do not include wave propagation effects rigorously. The hybrid methods are a combination of these two methods in which known aspects of the wave propagation are modeled deterministically while the unknown aspects are modeled stochastically.

The empirical Green's function method initially suggested by Hartzell (1978) was the first of many hybrid techniques. Rupture propagation and radiation pattern were specified deterministically, and the source radiation and propagation effects were included empirically by assuming that the motions observed from an aftershock contained this information. The methods proposed by Hadley and Helmberger (1980), Irikura (1983), and Heaton and Hartzell (1989) are modifications of Hartzell's method of summing empirical Green's functions. This method requires an adequate sampling in both distance and source depth of empirical Green's functions, which is difficult to obtain in most regions. In order to overcome this limitation, Hadley *et al.* (1982) proposed an approach which uses empirical source functions convolved with theoretical Green's functions. The approach described below, which is a modification of the Hadley *et al.* (1982) procedure, uses simplified Green's functions (potentials) which include only the effects of geometrical spreading and exclude the effects of radiation pattern and receiver function.

The procedure is illustrated schematically in figure 1. The fault is divided into discrete elements, and the motions from these elements are lagged and summed to simulate the propagation of rupture over the fault surface. A stochastic component is included in the velocities of fault slip and rupture propagation to simulate heterogeneity in rupture dynamics. Large scale asperities are introduced by varying the slip distribution over the fault surface.

The starting equation for the method is the representation theorem integral (Aki and Richards, 1980, eqn. 14.1) which gives the elastic displacement $\underline{u}$ caused by a displacement discontinuity $|\underline{u}\ (\underline{\xi},\tau)|$ across an internal surface Σ as

$$u_i(\underline{x},t) = \int_{-\infty}^{\infty} d\tau \int_{\Sigma} | u_j(\underline{\xi},\tau) | c_{jkpq} G_{ip,q}(\underline{x},t;\underline{\xi},\tau) \nu_k d\Sigma(\underline{\xi}) \qquad (1)$$

where c_{jkpq} are the elastic constants; G_{ip} is the Green function and $\hat{\nu}$ is unit normal to the fault surface. The $\underline{\xi}$ represents a point on the fault plane and $\underline{x}$ is the observation point. In the far-field, the above integral can be written as

$$\underline{U}(\underline{x},t) = \int_0^L \int_0^W \dot{D}(\xi_1,\xi_2,t) * \underline{G}(\underline{x},\xi_1,\xi_2,t) d\xi_1 d\xi_2 \qquad (2)$$

where $\underline{\xi} = (\xi_1,\xi_2)$ is the point on the fault plane, L is the fault length, W is the fault width, D is slip time history and G is the impulse response of the medium, and * represents a convolution. When we use the above equation to calculate the ground motion due to a large fault, we divide the fault plane into small elements, called subfaults. Assuming that we break up the fault plane into l elements (of length ΔL) along the length and m elements (of width ΔW) along the width of the fault plane, the above integral reduces to the following form

$$\underline{U}(\underline{x},t) = \sum_{i=1}^{l} \sum_{j=1}^{m} \int_0^{\Delta L} \int_0^{\Delta W} \dot{D}(\xi_1,\xi_2,t-\tau_r^{ij}) * \underline{G}(\underline{x},\xi_1,\xi_2,t) d\xi_1 d\xi_2 \qquad (3)$$

where τ_r^{ij} is the time that the rupture front takes to propagate from the hypocenter to the fault element (i,j). The propagation time from the element (i,j) to the observation point is included in the Green's function.

Hadley and Helmberger (1980) and Irikura (1983) pointed out the need to take into account the difference between the dislocation rise time of the large event and that of the small event. Based on a Haskell type self-similar kinematic source model, we need to add as many sources per subfault as the ratio of the rise time of the large event to that of the subevent from which the source function is derived. Then the above equation reduces to the following form

$$\underline{U}(\underline{x},t) = \sum_{i=1}^{l} \sum_{j=1}^{m} \sum_{k=1}^{nsrc} \int_0^{\Delta L} \int_0^{\Delta W} \dot{D}(\xi_1,\xi_2,t-\tau_r^{ij}-(k-1)\tau_e) * \underline{G}(\underline{x},\xi_1,\xi_2,t) d\xi_1 d\xi_2 \qquad (4)$$

where *nsrc* is the number of subsources per subfault given by $nsrc = \tau_o / \tau_e$, where τ_o and τ_e represent the rise time of the large event and the subevent respectively.

The simulated motion of the large event is then the summation of contributions from l fault elements along strike, m fault elements down dip, and *nsrc* source functions lagged in time on each fault element. If l, m and *nsrc* are numerically identical, then the subevent and the large event will have self-similar scaling (Irikura, 1983). It would be only by chance that the actual subevent and large event that we are working with would obey a single self-similar scaling relation exactly, and so this condition cannot usually be met and in general need not be met. In our simulations of both the Michoacan and Valparaiso earthquakes we have not met this requirement. However, for both events we have approximately satisfied the condition for maintaining self-similarity in spectral shape between the subevent and the large event based on an ω^2 scaling relation (Joyner and Boore, 1986). The condition is that the total number of subevents added be the four-thirds power of the moment ratio of the large event to the subevent.

Although the form of the radiated source spectrum may be specified deterministically, high frequency details are generally unknown and are therefore included empirically through the empirical source function. The empirical source function is derived from a strong motion recording close to a smaller event that has been corrected by a simplified Green's function. The correction that is most consistent with the usage intended for the source functions is a deconvolution of the recording with a theoretical Green's function from the source function event to the receiver. Due to zeros in the spectrum, however, deconvolution is typically unstable. Since the source function recordings are from horizontal distances of about one source depth, the synthetic response potentials are simple (usually a step function). In this case, the deconvolution amounts to division by a constant, G_o, which is the amplitude of the derivative of the step function. For a recorded seismogram, $S(t)$, the corrected empirical source function is therefore

$$S_E(t) = \frac{S(t)}{G_o}. \qquad (5)$$

G_o can be measured directly, but it is preferable to estimate G_o by comparing the maximum amplitude of the seismogram with its maximum after convolution with the step function derivative:

$$G_o = \frac{\max(S(t)*G(t))}{\max(S(t))} \tag{6}$$

where $G(t)$ corresponds to the time derivative of $\phi(t)$, $\Omega(t)$, or $\chi(t)$ defined in equation 8 below, and computed for the source function event-to-receiver geometry and velocity structure. If the synthetic response function is too complex to allow this approximate correction, we exclude the observed record from those considered as empirical source functions.

The empirical source functions also include an estimate of the frequency-dependent receiver functions. That is, they include the angular decomposition of the P, SV and SH wavefields onto vertical, radial and tangential components (P_Z, P_R, SV_Z, SV_R, SH), as well as amplification effects due to the medium properties at the surface. Since the velocity structure at the strong motion site for the large event may be different from the receiver structure of the empirical source functions, and since incidence angles can be quite different, a correction must be applied to the estimated receiver functions. In the simulation procedure, this correction is performed by multiplying the empirical source function by the ratio of theoretical whole-space receiver functions. For windowed empirical source functions denoted by P_Z, P_R, SV_Z, SV_R and SH_T, the corrected source functions are

$$P'_Z = \frac{1}{2}\left(\frac{\alpha_1 \cos i_2}{\alpha_2 \cos i_1}\right) P_Z + \frac{1}{2}\left(\frac{\alpha_1 \cos i_2}{\alpha_2 \sin i_1}\right) P_R$$

$$P'_R = \frac{1}{2}\left(\frac{\alpha_1 \sin i_2}{\alpha_2 \cos i_1}\right) P_Z + \frac{1}{2}\left(\frac{\alpha_1 \sin i_2}{\alpha_2 \sin i_1}\right) P_R$$

$$SV'_Z = \frac{1}{2}\left(\frac{\beta_1 \sin i_2}{\beta_2 \sin i_1}\right) SV_Z + \frac{1}{2}\left(\frac{\beta_1 \sin i_2}{\beta_2 \cos i_1}\right) SV_R \tag{7}$$

$$SV'_R = \frac{1}{2}\left(\frac{\beta_1 \cos i_2}{\beta_2 \sin i_1}\right) SV_Z + \frac{1}{2}\left(\frac{\beta_1 \cos i_2}{\beta_2 \cos i_1}\right) SV_R$$

$$SH'_T = \left(\frac{\beta_1 \sin i_2}{\beta_2 \sin i_1}\right) SH_T$$

where α_1, β_1 and i_1 are the P and S velocities and incidence angle at the source function receiver and α_2, β_2 and i_2 are similar parameters at the strong motion site of the simulated earthquake.

The empirical source function contains several effects in addition to that of the source. These include anelastic absorption (Q), unmodeled wave propagation effects such as scattering, and local site response. Our knowledge of the Q structure of subduction zones is sufficiently poor, and the dependence of t* on path length is sufficiently weak, that we make the simplifying assumption that the absorption present in the empirical source function adequately represents the absorption along the paths between all fault elements and the site. We represent the site effect empirically by using source functions derived from strong motion recordings from the desired site category (rock or soil).

Simplified Green's functions for each fault element are computed using the method of generalized rays

(Helmberger and Harkrider, 1978). The response is computed for a point source located at the center of the fault element with propagation through a plane-layered medium. Rays corresponding to the direct, upgoing P and S waves as well as primary reflections from each layer interface beneath the source are included. Mode conversions, reverberations and surface waves are not included. Since the radiation pattern and receiver function are implicitly included in the empirical source function, the synthetic Green's functions do not contain these factors. The Green's functions are thus essentially the response of the medium for P, SV and SH potentials. Specifically, the Green's functions are given by the equations

$$P: \qquad \phi(t) = \frac{M_0}{4\pi\rho_0\pi}\frac{1}{\pi}\left(\frac{2}{r}\right)^{\frac{1}{2}}\left[\frac{1}{\sqrt{t}} * \sum_{i=1}^{n} \Im m\left(\frac{\sqrt{p}}{\eta_\alpha}\Pi(p)\frac{dp}{dt}\right)_i\right]$$

$$SV: \qquad \Omega(t) = \frac{M_0}{4\pi\rho_0\pi}\frac{1}{\pi}\left(\frac{2}{r}\right)^{\frac{1}{2}}\left[\frac{1}{\sqrt{t}} * \sum_{i=1}^{n} \Im m\left(\frac{\sqrt{p}}{\eta_\beta}\Pi(p)\frac{dp}{dt}\right)_i\right] \qquad (8)$$

$$SH: \qquad \chi(t) = \frac{M_0}{4\pi\rho_0\pi}\frac{1}{\pi}\left(\frac{2}{r}\right)^{\frac{1}{2}}\left[\frac{1}{\sqrt{t}} * \sum_{i=1}^{n} \Im m\left(\frac{\sqrt{p}}{\eta_\beta}\Pi(p)\frac{dp}{dt}\right)_i\right]$$

where $\eta_c = \sqrt{(1/c)^2 - p^2}$, where $c = \alpha$ or β, and the quantity in brackets is evaluated over the Cagniard contour for each of the n rays. Three (P, SV and SH) step responses are computed for each fault-element site pair. The ray parameter of the first arriving ray (typically the upgoing direct ray) is used for the receiver function correction in the simulation procedure.

We chose not to include the radiation pattern in the Green's function in the present application because the empirical source functions that we use were recorded at distances comparable to the fault dimensions of the aftershocks, and thus are expected to represent an averaged radiation pattern. There is some evidence that the coherence of the radiation pattern becomes weaker as periods become shorter than about one-half sec (Liu and Helmberger, 1985), although the coherence of total S amplitude does not appear to decrease as much as that of SH and SV motions (Vidale, 1989). This period-dependent coherence of the radiation pattern can be represented empirically if a large number of empirical source functions is available (Wald *et al.*, 1988). However, as yet there is not a large enough set of recordings of a moderate magnitude subduction earthquake to permit this approach to be implemented in a subduction zone.

Each fault element begins to radiate energy when the rupture front reaches that element. In order to avoid artificial periodicities due to the discretization of the fault plane, and in order to approximate irregularities in rupture propagation, we have incorporated a stochastic component in the time at which each fault element begins to radiate. As illustrated in figure 2, the turn-on time, T_o, includes a random number R_G with a Gaussian probability distribution centered about $(t_b - t_a)/2$. The probability that T_o is within (t_a,t_b) was set at the three standard deviation level, or a confidence level of 99.7%.

The form of the slip function at each point on the fault is assumed to be a simple ramp (following Haskell, 1964), parameterized by static slip and rise time. The slip function of the large event is built up by the summation of *nsrc* empirical source functions as described above. In order to avoid an artificial periodicity corresponding to the rise time of the source function, and to simulate roughness or variation in the instantaneous slip rate, a stochastic component is included in the slip function. Accordingly, in addition to lagging the source functions at uniform multiples of the rise time T_e of the source function, a random lag is also included as shown in figure 2. The probability that the initiation time t_{si} of a given source function is within (t_i, t_{i+1}) was set at the three standard deviation level.

An important aspect of the source at high frequencies is the characterization of fault heterogeneity or roughness. The heterogeneity may be manifested as local variations in static slip, slip rate, or rupture velocity. It is possible that all three are interdependent and that each contributes significantly to the high frequency radiation.

There is little agreement, however, in exactly how these characteristics are physically related, and it is unreasonable to allow them to vary independently. We have therefore opted to implement a simple asperity model of fault roughness in which static slip varies in a deterministic manner over the rupture surface, while variations in slip rate and rupture velocity are incorporated stochastically. To specify the slip distribution on the fault, each element is assigned a weighting factor which is a discretization of the static slip contours, normalized to preserve total seismic moment.

We wish to determine whether models of heterogeneous slip in subduction earthquakes derived by other investigators from the analysis of teleseismic and near-source velocity seismograms are also consistent with the shorter period motions of the recorded accelerograms. The 1985 M_w=8 Michoacan and Valparaiso earthquakes were selected for this test based on the geometrical similarities with Cascadia cited above and because estimates of the spatial distribution of slip on the rupture surface were available in each case. For the Michoacan earthquake, Houston and Kanamori (1986) showed that short period (1 sec) teleseismic waves were generated preferentially from the same regions of the fault plane as long period (10-50 sec) waves. This suggests that higher frequency (less than 1 sec period) strong ground motion may have also been preferentially generated from these regions.

Implementation of the simulation procedure requires estimates of a number of source parameters, some of which (such as the rupture dimensions) are known for the specific earthquake in question, and others of which (such as rupture velocity) are assigned reasonable fixed values. In principle, there are no free parameters involved in the procedure. This was the case for the Michoacan earthquake, for which good estimates of the source parameters (including the slip duration and rise time) were available from other studies. In the case of the Valparaiso earthquake, there was no available estimate of the slip duration, and hence it was treated as a free parameter to be optimized. Also, the slip distribution model of the Valparaiso earthquake derived from teleseismic analysis was perturbed slightly to improve the fit between recorded and simulated accelerograms.

To use predicted strong ground motions computed by the simulation procedure in engineering analyses, an estimate of their uncertainty is required that is analogous to that given for empirical ground motion prediction equations. The total uncertainty in the predicted strong ground motion should include all sources of uncertainty: modeling uncertainty (describing the adequacy of the simulation procedure in representing the processes that generate strong ground motions); random uncertainty (describing event-to-event and station-to-station variability that is not accounted for in the source and wave propagation models); and parametric uncertainty (describing the uncertainty in the values of source parameters of future earthquakes).

A procedure for estimating these uncertainties was developed by Abrahamson *et al.*, (1990, 1991). The modeling and random component of uncertainty is estimated from the misfit between recorded and simulated ground motions for a suite of earthquakes. The contribution of parametric uncertainty to the misfit between recorded and simulated motions is assumed to be negligible if the gross fault parameters of the suite of earthquakes are known. The parametric uncertainty is estimated in the process of simulating ground motions in the Puget Sound - Portland region by varying unconstrained model parameters in the simulations. It is measured from the variability in the ground motions due to these variations in parameter values. The overall uncertainty is obtained by combining the modeling and random uncertainty with the parametric uncertainty.

MODELING AND RANDOM UNCERTAINTY: SIMULATION OF MICHOACAN AND VALPARAISO EARTHQUAKES

Our first step is to test the simulation procedure against recorded accelerograms of the 1985 M_w=8.0 Michoacan, Mexico and Valparaiso, Chile subduction earthquakes in preparation for applying the simulation procedure in the Puget Sound - Portland region. Strong motion recordings of magnitude 7 aftershocks of the Michoacan and Valparaiso earthquakes, corrected for wave propagation using a simple model, were used as empirical source functions. Green's functions were calculated using generalized rays in layered structures.

We found that models of heterogeneous slip on the fault planes derived by Mendoza and Hartzell (1988) and Houston (1987) for the Michoacan and Valparaiso earthquakes respectively from the analysis of near-source and teleseismic velocity seismograms are also consistent with the higher frequency motions of the recorded accelerograms. This is illustrated in figure 3, in which the variations in the envelopes of the recorded accelerograms of the Michoacan earthquake from station to station are reproduced in the simulated accelerograms, reflecting the

influence of the slip distribution and the southeasterly direction of rupture propagation on the recorded accelerograms. The simulations, which use the Caleta de Campos (rock site) source function, show close agreement in overall duration of strong motion, frequency content, and peak acceleration. Strong motion simulations using a uniform slip model do not produce the two large wave packets in the accelerogram recorded at La Villita, but these are produced by the two large asperities in the slip model of Mendoza and Hartzell (1988). The uniform slip model produces accelerograms having longer durations and lower peak amplitudes than those of both the recorded data and the asperity model simulations. A comparison of recorded and simulated response spectra averaged over these five rock site stations in figure 4a also shows good agreement.

In contrast to the Michoacan earthquake, the Valparaiso earthquake was extensively recorded on soil sites, and the motions recorded on soil were significantly larger than those on rock. This is shown in the response spectra for the Valu rock site (fig. 4b) and the average of five soil sites (fig. 4c). This difference between soil and rock motions is also obtained in the simulated ground motions, as shown in figures 4b and 4c. The simulations for the two different site conditions were generated using the Valu (rock site) source function in simulations for rock sites and the neighboring Vina (soil site) source function in simulations for soil sites. The large peak in the response spectrum shown in figure 4b is due to a peak in the spectrum of the Valu (rock site) source function at that period, and the peak in the response spectrum shown in figure 4c is due to a peak in the spectrum of the Vina (soil site) source function at that period. Using a uniform slip model produces accelerograms having longer durations and lower peak amplitudes than those of both the recorded data and the asperity model simulations. The modeling of the Michoacan and Valparaiso earthquakes is described in some detail in Somerville *et al.* (1991).

Quantitative measures of the agreement between the recorded and simulated response spectra were used as estimates of modeling and random uncertainty. The response spectra of the simulated motions generally have little or no significant bias in the period range of 0.05 to 2 sec for both earthquakes, and the peak accelerations, durations, and envelope shapes of the time histories are in generally good agreement with the recorded motions. We found that empirical source functions from rock sites in Mexico and Chile could be used interchangeably, and that the uncertainty associated with using the rock site source functions was not significantly changed when source functions derived from one subduction zone were used to simulate strong ground motions in the other subduction zone. The standard error associated with the use of each of the empirical source functions, expressed as the natural logarithm of spectral acceleration, is shown in figure 5. The windowed time series, response spectra, and model bias for each of the empirical source functions is shown in Somerville *et al.* (1991).

ESTIMATION OF SUBDUCTION EARTHQUAKE GROUND MOTIONS IN THE PUGET SOUND - PORTLAND REGION

The simulation procedure was next applied to estimate strong ground motions in the Puget Sound - Portland region from hypothesized M_w=8 subduction earthquakes on the Cascadia subduction zone. Fault models for the western Washington and Oregon regions and seismic velocity structure models were developed from published regional studies. The surface projections of the two fault models, subdivided into the fault elements used in the simulation procedure, are shown in figure 6a. A cross section normal to the strike of the western Washington subduction zone delineating the rupture surface is shown in figure 6b. The rupture surfaces of the Michoacan and Valparaiso earthquakes are superimposed on this cross section. The western Washington model has a dip of 11°, which is similar to the 14° dip of the Michoacan plane, while the Oregon model has a dip of 21°, which is similar to the 25° dip of the Valparaiso plane. The western Washington and Oregon fault models have different downdip width, fault length, and depth to top of fault (assumed to be 17 km and 13 km respectively), as shown in figure 6a.

The plate interface is not imaged directly from seismicity data because it is historically aseismic. Instead, the geometry of the plate interface is derived from offshore refraction profiles (Taber and Lewis, 1986) and the inclined zone of earthquake hypocenters within the shallow (<30 km) Juan de Fuca plate. Identifying the deepest (and easternmost) extent of potential rupture on the plate interface is the most critical geometrical source parameter for estimating ground motions in the Puget Sound - Portland region, since this controls the closest approach of the rupture surface. There is general agreement that the subducting plate at depth is arched beneath Puget Sound, as shown by the 54 km depth contour in figure 6a (Crosson and Owens, 1987; Weaver and Baker, 1988). To delineate the shallow plate interface, we have used the structure of Weaver and Baker (1988) which is constrained closely by

the hypocentral data, and in which the 40 km depth contour is not arched. Assuming that the seismicity is confined beneath the oceanic Moho, then the 40 km depth contour on the plate interface, which is inferred to be the easternmost edge of the rupture surface, lies about 50 km west of Puget Sound, as shown in figure 6. However, Crosson and Owens (1987) preferred the interpretation that the shallow plate interface is arched. This interpretation places the eastern margin of the potential rupture surface directly beneath Puget Sound. The result of using this interpretation can be approximated by moving our ground motion grid (described below) 50 km to the east, which greatly increases the ground motions in Puget Sound.

A two-dimensional (2-D) velocity profile across the subduction zone derived by Spence *et al.* (1985) is shown in figure 7. We have approximated this 2-D model using 1-D models for each of the source depths (one at the center of each fault element) used in the simulations. The models for the different source depths on the plate interface, derived from the velocity structure shown in figure 6b, each have the oceanic Moho at a depth of 6 km below the source. The adequacy of approximating the 2-D model by these 1-D models was tested by comparing generalized ray Green's functions computed in these models with finite difference Green's functions for the 2-D model shown in figure 7. In both calculations, which are compared in figure 8, the largest phases are the direct S wave and the S wave that is critically reflected from the Moho of the subducting plate. Accordingly, we used the simplified 1-D velocity model of the region, taking the changing depths of the plate interface and the Moho of the subducting plate into account.

Although the dip of the Oregon fault model is nearly twice that of the western Washington model, the ground motions for the two regions are not very different. Given the location of the potential rupture surface that we have assumed, the largest cause of uncertainty in estimated ground motions in the Puget Sound - Portland region is due to uncertainty in the distribution of slip with depth on the plate interface. We performed simulations for three generalized asperity models in which 60% of total moment is released in the upper, middle and lower third of the fault (termed shallow, middle and deep models respectively). The size and strength of the asperities and their distribution along strike in the western Washington and Oregon fault models is consistent with the slip distributions found for the Michoacan and Valparaiso earthquakes respectively.

Ground motion simulations were computed at the grid of points shown as open squares in figure 6. The grid consists of lines of points, labelled *a* through *g*, that are parallel to the strike of the fault and 20 km apart. The dependence of the simulated time histories for rock sites on the depth of the asperity is shown in figure 9 for the western Washington fault model and in figure 10 for the Oregon fault model. The time histories shown are from the profile of stations that intersects the surface projection of the fault near the maximum slip of the asperity, and are therefore representative of maximum ground motions that would be selected in a deterministic analysis of seismic hazard. As the asperities become deeper, they become closer to the grid of stations, causing the peak accelerations on the grid to increase, as shown in figure 11a. Also, as a result of the increasing depth of the asperity, the attenuation of peak acceleration becomes more gradual. The variability of peak ground acceleration over rows *a* - *g* of the Oregon grid is shown in figure 12. In addition to the variability with distance which we have already described, there is variability due to along-strike variations in slip and to the bilateral propagation of rupture across the fault surface.

The peak acceleration values, averaged along fault strike, for all of the simulations generated in this study are given in tables A1 and A2 for the western Washington and Oregon fault models respectively. The values are broken down according to the source function used (Cal and Valu: rock; and Vina: soil); the asperity model (shallow, middle and deep); and the station row (*a* through *g*). Both closest distance and distance to the asperity are given for each pair of peak horizontal acceleration values.

If we measure closest distance to the asperity instead of closest distance to the rupture surface, the attenuation curves for the three asperity depths are not significantly different, as shown in figure 11b. The attenuation is described by the equation:

$$\ln(PGA) = a + b \ln(r + c) + ds \qquad (9)$$

where r is distance to the nearest asperity in km, PGA is maximum horizontal acceleration in g, and s is the site term, 1 for soil and 0 for rock sites. A least-squares solution, averaged over the two fault dips and three asperity depths, yields a=15.5, b=-3.33, c=128 and d=0.79 with a standard error of 0.32 (natural logarithm of peak

acceleration). All parameters are significant at the 95% confidence level. This relation is only appropriate for $25<r<175$ km and $M_w=8$. Combining the modeling and random standard error of 0.51, derived from the fit to the Michoacan and Valparaiso earthquakes, with the parametric uncertainty value of 0.32, yields a total standard error of 0.60.

At present we do not know the depth at which slip on the plate interface of the Cascadia subduction zone will be concentrated if there is a large subduction earthquake. To make ground motion predictions, we would then use the closest distance to the rupture surface instead of the closest distance to the asperity. A regression with the same functional form as that given above yields a=2.8, b=-1.26, c=0 and d=0.79 with a standard error of 0.40. The increase in the standard error from 0.32 to 0.40 reflects the variability in ground motion amplitude due to uncertainty in the depth of slip. The total standard error is 0.65. This relation is only appropriate for $30<r<100$ km and $M_w=8$. At closer distance, the slope of the attenuation relation would decrease, as suggested by the trend of the Portland values for r~30 km in figure 13.

In figure 13, we plot the median values of the three asperity models against empirical attenuation relations based on average properties of global recordings of subduction earthquakes. Youngs *et al.* (1988), and a more applied study by the same authors, WPPSS (1988), present separate attenuation relations for rock and soil sites. The separation between the empirical rock and soil curves is close to the $e^{0.79}$ term in our attenuation relations (soil-site peak accelerations ~2.2 times larger than rock-site peaks). The slopes of the attenuation relations, however, are considerably different: our predicted PGA values at close distance (30-40 km) are larger than the empirical result, and the decay of PGA with distance is more rapid in our simulations.

Fukushima and Tanaka (1990) have shown that the strong correlation between magnitude and the decay of PGA in the empirical Japanese data has led to attenuation relations with artificially slow PGA attenuation when the data are combined in a general non-stratified regression method, like that used by Youngs *et al.* (1988). When a two-step stratified regression method (Fukushima and Tanaka, 1990) is used to isolate the magnitude-slope dependence, the decay of PGA with distance is found to be quite similar to standard empirical attenuation relations derived from crustal earthquake data (Campbell, 1981; Joyner and Boore, 1988), although values of PGA for a given distance and magnitude are different. The slope of our PGA attenuation relation is similar to that of Campbell (1981), Joyner and Boore (1988), and the two-step regression result of Fukushima and Tanaka (1990).

Additionally, in the Youngs *et al.* (1988) study, all data closer than 40 km (M_w=7.8-8.2) are from the 1985 Michoacan mainshock, which had anomalously shallow slip for a subduction zone earthquake (Tichelaar and Ruff, 1989), yielding relatively weak motions for a given distance to the rupture surface as shown in figure 11a. Further, it appears that site response at the Mexican strong motion stations (deamplification at La Union and Zihuatanejo near the Michoacan source region and amplification at Papanoa, further to the southeast; Castro *et al.*, 1990) may have caused flattening of the attenuation relation. The Oregon fault model has slightly larger motions than the western Washington model for a given value of closest distance to the fault. This is because the steeper dip and narrower fault width of the Portland model bring more of the fault into close proximity to the site.

Figure 14 shows the smoothed median 5% damped PSV curves for rock for both the western Washington and Oregon models; these have been averaged over the three asperity models for each of the lines of stations (*a* - *g*) shown in figure 6. They are also averages over separate simulations generated using the two rock-site source functions (Caleta, Mexico and Valparaiso, Chile). We have estimated the uncertainty in the response spectral estimates using the procedure developed by Abrahamson *et al.* (1990, 1991). An estimate of parametric uncertainty was derived from the variability in ground motions at a given closest distance from the fault due to differences in the position of the station along fault strike and in the along-strike and down-dip location of the asperity. An estimate of modeling and random uncertainty was derived from the misfit between recorded and simulated motions of the 1985 Michoacan and Valparaiso earthquakes described above and illustrated in figure 5. The overall uncertainty, derived by combining these two uncertainty estimates, is represented in the 84th percentile response spectra shown in figure 14. Inclusion of these uncertainty estimates in the ground motion predictions allows them to be used in probabilistic seismic hazard calculations for the Puget Sound - Portland region.

The median and 84th percentile response spectral velocity values for rock sites (average of the Cal and Valu source functions), averaged along fault strike, are given in tables A3 and A4 for the western Washington and Oregon fault models respectively. The values are given for each station line number (*a* through *g*); the closest distance for each line is given in tables A1 and A2.

In figure 15a, we compare the median soil-site simulated response spectrum for the Seattle - Portland area with estimates derived in two empirical studies. The first was derived by Crouse *et al.* (1988) using regression methods (30 km source depth, 120 km to center-of-energy-release). The second was derived by Heaton and Hartzell (1989) from averages of strong motion recordings from magnitude 7.6 to 8.2 subduction events in the epicentral distance ranges of 50-100 km and 100-150 km. The simulated response spectral estimates are for the shallow asperity model, the deep asperity model, and for the average of the three asperity models for the western Washington fault model for line *f*, which includes Seattle. The empirical estimates generally span the range between the estimates for the average and shallow asperity models derived from numerical modeling. The soil site simulations were generated using the Vina soil-site source function from the Valparaiso aftershock. We have not predicted motions at periods longer than 1 sec, because these motions are expected to be strongly influenced by the deep 3-D structure of the Puget Trough and Portland Basin and therefore strongly site-dependent, and not well represented by the site conditions of the Vina site.

Strong motions were recorded in the Puget Sound region from two Wadati-Benioff zone earthquakes that occurred in 1949 and 1965. The locations of these events are shown as stars in the cross-section of the subduction zone in figure 6b. They occurred within the lower part of the subducting Juan de Fuca plate beneath Seattle and Tacoma, at depths greater than the downdip limit of rupture (40 km) of the plate interface in our hypothesized fault models. It is of interest to compare these recorded motions with the motions we have simulated for a magnitude 8 subduction earthquake. In figure 15b, we show the averaged PSV response of 10 horizontal recordings from the two Wadati-Benioff zone earthquakes: Seattle and Olympia records for 13 April 1949 (magnitude 6.5), and Seattle, Tacoma, and Olympia records for 29 April 1965 (magnitude 7.1). The simulated PSV result for the magnitude 8 subduction earthquake is the average soil-site result for the three locations weighted accordingly. The estimated response spectral values for the subduction earthquake are about a factor of two larger between 1 and 10 Hz than those recorded during the 1949 and 1965 events. The duration of strong motion is expected to be longer for the subduction earthquake (rock site: 45-60 sec vs. 10-15 sec), and the long period motions more than a factor of two larger.

CONCLUSIONS

Models of heterogeneous slip distribution on the fault planes derived by Mendoza and Hartzell (1988) and Houston (1987) for the Michoacan and Valparaiso earthquakes respectively from the analysis of near-source and teleseismic velocity seismograms are also consistent with the higher frequency motions of the recorded accelerograms. The simulated ground motions showed close agreement in overall duration of strong motion, frequency content, and peak acceleration of the recorded motions of both events. Quantitative measures of the agreement between the recorded and simulated response spectra were used as estimates of modeling and random uncertainty.

Identifying the deepest (and easternmost) extent of potential rupture on the plate interface is the most critical geometrical source parameter for estimating ground motions in the Puget Sound region, since this controls the closest approach of the rupture surface. We have used the model of Weaver and Baker (1988) which is closely constrained by the hypocentral data. It places the 40 km depth contour on the plate interface, inferred to be the easternmost edge of the rupture surface, 50 km west of Puget Sound. However, Crosson and Owens (1987) favor the interpretation that the shallow plate interface, as well as the deeper plate interface beneath Puget Sound, is arched. This interpretation places the eastern margin of the potential rupture surface directly beneath Puget Sound, and results in much larger ground motion estimates in Puget Sound.

Given the location of the potential rupture surface that we have assumed, the largest cause of uncertainty in estimated ground motions in the Puget Sound - Portland region is due to uncertainty in the distribution of slip (asperities) with depth on the plate interface. As the asperities become deeper, they become closer to the grid of stations, causing the ground motions in the Puget Sound - Portland regions to increase. As a result of the increasing depth of the asperity, the attenuation of peak acceleration with distance becomes more gradual. Although the dip of the Oregon fault model is nearly twice that of the western Washington model, the ground motions for the two regions are not very different.

We have estimated the uncertainty in response spectral estimates using the procedure developed by

Abrahamson *et al.* (1990, 1991). An estimate of parametric uncertainty was derived from the variability in ground motions at a given closest distance from the fault due to differences in the position of the station along fault strike and in the along-strike and down-dip location of the asperity. An estimate of modeling and random uncertainty was derived from the misfit between recorded and simulated motions of the 1985 Michoacan and Valparaiso earthquakes. The overall uncertainty, derived by combining these two uncertainty estimates, is represented by 84th percentile response spectra. These uncertainty estimates allow the ground motion estimates to be used in probabilistic seismic hazard calculations for the Puget Sound - Portland region.

ACKNOWLEDGMENTS

This work was supported by the U.S. Geological Survey, Department of the Interior, under award #14-08-0001-G1516. Mrinal Sen assisted in the analysis of the Valparaiso earthquake and Dave Wald assisted in the early stages of the Michoacan work. Reviews by Stephen Hartzell, Robert Youngs, and Albert Rogers are gratefully acknowledged.

REFERENCES

Abrahamson, N. A., Somerville, P. G., and Cornell, C. A., 1990, Uncertainty in numerical strong motion predictions, Proceedings of the 4th U.S. National Conference on Earthquake Engineering, Palm Springs, p.407-416.

Abrahamson, N. A., Somerville, P. G., and Cornell, C. A., 1991, Uncertainty in numerical strong motion predictions for engineering applications: Bulletin of the Seismological Society of America, [submitted for publication].

Adams, J., 1990, Paleoseismicity of the Cascadia subduction zone: evidence from turbidites off the Oregon-Washington margin, Tectonics, v.9, p.569-583.

Aki, K., 1968, Seismic displacements near a fault, Journal of Geophysical Research, v.73, p.5359-5376.

Aki, K., and Richards, P. G., 1980, Quantitative Seismology: Theory and Methods, W.H. Freeman and Company, San Francisco.

Atwater, B., 1987, Evidence for great Holocene earthquakes along the outer coast of Washington state, Science, v.236, p.942-944.

Campbell, K. W., 1981, Near-source attenuation of peak horizontal acceleration: Bulletin of the Seismological Society of America, v.71, p.2039-2070.

Castro, R. R., Anderson, J. G., and Singh, S. K., 1990, Site response, attenuation, and source spectra of S-waves along the Guerrero, Mexico subduction zone: Bulletin of the Seismological Society of America, v.80, p.1481-1503.

Cohee, B. P., Somerville, P. G., and Abrahamson, N. A., 1991, Simulated ground motions for hypothesized M_w=8 subduction earthquakes in Washington and Oregon: Bulletin of the Seismological Society of America, v.81, p.28-56.

Crosson, R. S., and Owens, T. J., 1987, Slab geometry of the Cascadia subduction zone beneath Washington from earthquake hypocenters and teleseismic converted phases, Geophysical Research Letters, v.14, p.824-827.

Crouse, C. B, Vyas, Y. K., and Schell, B. A., 1988, Ground motions from subduction zone earthquakes: Bulletin of the Seismological Society of America, v.78, p.1-25.

Day, S. M., Stevens, J. L., and Barker, T. G., 1988, Ground motion simulations for thrust earthquakes beneath western Washington, Final Report submitted to Washington Public Power Supply System, Richland, Washington.

Fukushima, Y., and Tanaka, T., 1990, A new attenuation relation for peak horizontal acceleration of strong earthquake ground motion in Japan: Bulletin of the Seismological Society of America, v.80, p.757-783.

Hadley, D. M., and Helmberger, D. V., 1980, Simulation of strong ground motions: Bulletin of the Seismological Society of America, v.70, p.617-630.

Hadley, D. M., Helmberger, D. V., and Orcutt, J. A., 1982, Peak acceleration scaling studies: Bulletin of the Seismological Society of America, v.72, p.959-979.

Hanks, T. C., and McGuire, R. K., 1981, The character of high frequency ground motion: Bulletin of the Seismological Society of America, v.71, p.2071-2095.

Hartzell, S. H., 1978, Earthquake aftershocks as Green's functions, Geophysical Research Letters, v.5, p.1-4.

Hartzell, S. H., and Heaton, T. H., 1988, Failure of self-similarity for large (M_w>81/4) earthquakes: Bulletin of the Seismological Society of America, v.78, p.478-488.

Haskell, N. A., 1964, Total energy and energy spectral density of elastic wave radiation from propagating faults: Bulletin of the Seismological Society of America, v.54, p.1811-1841.

Haskell, N. A., 1969, Elastic displacements in the near-field of a propagating fault: Bulletin of the Seismological Society of America, v.59, p.865-908.

Heaton, T. H., and Kanamori, H., 1984, Seismic potential associated with subduction in the northwestern United States: Bulletin of the Seismological Society of America, v.74, p.933-941.

Heaton, T., and Hartzell, S., 1989, Estimation of strong ground motions from hypothetical earthquakes on the Cascadia subduction zone, Pure and Applied Geophysics, v.129, p.131-201.

Helmberger, D. V., and Harkrider, D. G., 1978, Modeling earthquakes with generalized ray theory, Proc. of IUATM Symposium: Modern Problems in Elastic Wave Propagation, John Wiley & Sons, Inc., New York, p.499-518.

Houston, H., and Kanamori, H., 1986, Source spectra of great earthquakes: teleseismic constraints on rupture process and strong motion: Bulletin of the Seismological Society of America, v.76, p.19-42.

Houston, H., 1987, Source characteristics of large earthquakes at short periods, Ph.D. Thesis, California Institute of Technology, 129 pp.

Irikura, K., 1983, Semi-empirical estimation of strong ground motions during large earthquakes, Bulletin of the Disaster Prevention Research Institute, Kyoto University, v.33, p.63-104.

Irikura, K., 1986, Prediction of strong acceleration motions using empirical Green's function, Proceedings of the 7th Japan Earthquake Engineering Symposium, p.151-157.

Joyner, W. B., and Boore, D. M., 1986, On simulating large earthquakes by Green's function addition of smaller earthquakes, in Earthquake Source Mechanics, American Geophysical Union Maurice Ewing Series no.6, S. Das *et al.* eds., p.269-274.

Joyner, W. B., and Boore, D. M., 1988, Measurement, characterization, and prediction of strong ground motion, in Earthquake Engineering and Soil Dynamics II - Recent Advances in Ground Motion Evaluation, American Society of Civil Engineers Geotechnical Special Publication 20, J.L. von Thun ed., p.43-102.

Kamiyama, M., 1988, Synthesis of strong motion accelerograms from small earthquake records by use of a scaling law of spectra, Structural Engineering / Earthquake Engineering, v.5, p.173-182.

King, K. W., Tarr, A. C., Carver, D. L., Williams, R. A., and Worley, D. M., 1990, Seismic ground-response studies in Olympia, Washington, and vicinity: Bulletin of the Seismological Society of America, v.80, p.1057-1078.

Liu, H.-L., and Helmberger, D. V., 1985, The 23:19 aftershock of the October 1979 Imperial Valley earthquake: more evidence for an asperity: Bulletin of the Seismological Society of America, v.75, p.689-708.

Mendoza, C., and Hartzell, S. H., 1988, Slip distribution of the 19 September 1985 Michoacan, Mexico earthquake: near-source and teleseismic constraints: Bulletin of the Seismological Society of America, v.79, p.655-669.

Singh, S. K., Ordaz, M., Anderson, J. G., Rodriguez, M., Quaas, R., Mena, E., Ottaviani, M., and Almora, D., 1989, Analysis of near-source strong-motion recordings along the Mexican subduction zone: Bulletin of the Seismological Society of America, v.79, p.1697-1717.

Spence, G. D., Clowes, R. M., and Ellis, R. M., 1985, Seismic structure across the active subduction zone of western Canada, Journal of Geophysical Research, v.90, p.6754-6772.

Somerville, P. G., Sen, M. K., and Cohee, B. P., 1991, Simulation of strong ground motions recorded during the 1985 Michoacan, Mexico and Valparaiso, Chile earthquakes: Bulletin of the Seismological Society of America, v.81, p.1-27.

Taber, J. J., and Lewis, B. T. R., 1986, Crustal structure of the Washington continental margin from refraction data: Bulletin of the Seismological Society of America, v.76, p.1011-1024.

Takemura, M. and Ikeura, T., 1988, A semi-empirical method using a hybrid of stochastic and deterministic fault models: simulation of strong ground motions during large earthquakes, Journal of Physics of the Earth, v.36, p.89-106.

Tichelaar, B. W., and Ruff, L. J., 1989, Shallow seismic coupling in the Mexican subduction zone [abs.], EOS, v.70, p.1208.

Vidale, J. E. (1989). Influence of focal mechanism on peak accelerations of the Whittier Narrows, California earthquake and its one aftershock, Journal of Geophysical Research, v.94, p.9607-9613.

Wald, D. J., Burdick, L. J., and Somerville, P. G., 1988, Simulation of acceleration time histories close to large earthquakes, in Earthquake Engineering and Soil Dynamics II - Recent Advances in Ground Motion Evaluation, American Society of Civil Engineers Geotechnical Special Publication 20, J.L. von Thun ed., p.430-444.

Weaver, C. S., and Baker, G. E., 1988, Geometry of the Juan de Fuca plate beneath Washington and northern Oregon from seismicity: Bulletin of the Seismological Society of America, v.78, p.264-275.

WPPSS (1988). Cascadia subduction zone: an evaluation of the earthquake potential and implications to WNP-3, Response to NRC questions 230.1 and 230.2, Washington Public Power Supply System, Richland, Washington.

Youngs, R. R., Day, S. M., and Stevens, J. L., 1988, Near field ground motions on rock for large subduction earthquakes, in Earthquake Engineering and Soil Dynamics II - Recent Advances in Ground Motion Evaluation, American Society of Civil Engineers Geotechnical Special Publication 20, J.L. von Thun ed., p.445-462.

Table A1: Median Peak Accelerations - Puget Sound Fault Model						
asperity model	line	asperity dist (km)	fault dist (km)	line average peak accel (g)		
				Cal H	Valu H	Vina H
Shallow	a	56.8	34.7	.201	.143	.369
	b	75.2	38.2	.157	.101	.273
	c	94.2	41.8	.118	.078	.211
	d	113.6	51.2	.093	.057	.155
	e	133.1	65.6	.071	.044	.119
	f	150.8	80.6	.056	.036	.100
	g	172.5	100.3	.045	.027	.077
Middle	a	34.7	34.7	.249	.186	.501
	b	45.3	38.2	.202	.142	.392
	c	60.9	41.8	.169	.115	.313
	d	78.5	51.2	.139	.094	.238
	e	97.0	65.6	.104	.069	.193
	f	114.1	80.6	.085	.052	.154
	g	135.3	100.3	.066	.042	.108
Deep	a	37.3	34.7	.260	.172	.460
	b	38.2	38.2	.240	.178	.462
	c	41.8	41.8	.226	.153	.414
	d	51.2	51.2	.195	.131	.334
	e	65.6	65.6	.158	.105	.279
	f	80.6	80.6	.140	.098	.250
	g	100.3	100.3	.109	.071	.197

Table A2: Median Peak Accelerations - Portland Region Fault Model						
asperity model	line	asperity dist (km)	fault dist (km)	line average peak accel (g)		
				Cal H	Valu H	Vina H
Shallow	a	28.2	28.2	.462	.289	.796
	b	43.9	32.9	.326	.218	.551
	c	62.2	39.3	.207	.142	.387
	d	81.2	49.1	.147	.090	.266
	e	100.7	63.9	.083	.058	.155
	f	120.3	80.9	.054	.038	.108
	g	140.0	99.0	.040	.027	.075
Middle	a	29.7	28.2	.312	.202	.551
	b	32.9	32.9	.317	.199	.533
	c	45.6	39.3	.196	.127	.351
	d	62.3	49.1	.173	.107	.309
	e	80.5	63.9	.122	.081	.231
	f	99.4	80.9	.093	.060	.161
	g	118.7	99.0	.070	.047	.131
Deep	a	47.0	28.2	.235	.158	.440
	b	38.5	32.9	.271	.190	.479
	c	39.3	39.3	.234	.161	.411
	d	49.1	49.1	.187	.131	.357
	e	63.9	63.9	.151	.099	.270
	f	80.9	80.9	.126	.084	.226
	g	99.0	99.0	.103	.070	.187

Table A3: Mean Spectral Velocity - Rock								
Puget Sound Fault Model								
	Period	a	b	c	d	e	f	g
Mean	0.030	0.93	0.77	0.64	0.52	0.40	0.33	0.25
	0.045	1.69	1.37	1.13	0.93	0.71	0.59	0.45
	0.056	2.40	1.95	1.61	1.33	1.01	0.85	0.65
	0.069	3.43	2.79	2.31	1.91	1.45	1.23	0.93
	0.087	4.90	3.98	3.33	2.73	2.09	1.77	1.34
	0.108	7.07	5.73	4.83	3.91	3.03	2.56	1.94
	0.135	10.14	8.14	6.89	5.53	4.33	3.65	2.74
	0.168	13.85	11.08	9.30	7.45	5.84	4.90	3.68
	0.210	17.72	14.29	11.90	9.46	7.44	6.17	4.65
	0.261	21.51	17.56	14.64	11.50	9.10	7.41	5.67
	0.326	24.58	20.20	16.90	13.20	10.50	8.43	6.56
	0.407	25.90	21.39	17.92	14.00	11.15	8.89	7.02
	0.507	26.05	21.92	18.35	14.36	11.47	9.09	7.33
	0.632	26.66	23.01	19.33	15.17	12.23	9.58	7.91
	0.789	27.93	24.32	20.65	16.30	13.18	10.22	8.44
	0.984	29.09	25.12	21.36	17.15	13.73	10.56	8.51
	1.227	30.11	25.79	21.56	17.59	14.14	10.87	8.57
	1.530	30.20	25.76	21.37	17.31	14.43	11.21	8.94
	1.908	27.68	23.44	19.76	15.64	13.52	10.78	8.90
	2.380	24.00	20.21	17.26	13.29	11.64	9.60	8.07
	2.968	20.98	17.59	15.13	11.56	9.95	8.36	7.02
	3.701	16.16	13.58	11.72	9.12	7.56	6.36	5.35
84th	0.030	1.73	1.46	1.22	1.01	0.78	0.67	0.51
perc	0.045	3.36	2.59	2.13	1.90	1.36	1.19	0.87
	0.056	4.86	3.78	3.12	2.78	1.99	1.75	1.27
	0.069	7.03	5.48	4.56	4.05	2.90	2.57	1.86
	0.087	10.15	7.93	6.66	5.87	4.25	3.76	2.71
	0.108	14.72	11.45	9.73	8.48	6.21	5.46	3.93
	0.135	20.77	16.03	13.66	11.85	8.72	7.65	5.49
	0.168	27.37	21.04	17.79	15.48	11.33	9.93	7.13
	0.210	34.17	26.55	22.14	19.25	14.00	12.20	8.83
	0.261	41.57	32.75	27.14	23.34	16.99	14.60	10.75
	0.326	48.12	37.88	31.37	26.68	19.56	16.53	12.42
	0.407	50.56	39.60	32.69	27.52	20.37	16.91	13.02
	0.507	49.29	38.93	31.83	26.54	19.90	16.26	12.99
	0.632	48.18	38.49	31.25	25.92	19.79	15.88	13.27
	0.789	49.03	39.09	31.99	26.61	20.45	16.11	13.78
	0.984	51.75	41.02	33.71	28.23	21.64	16.74	14.15
	1.227	56.18	44.54	35.98	29.75	23.43	17.89	14.90
	1.530	59.08	47.02	37.72	30.00	25.05	19.25	16.23
	1.908	54.91	44.14	36.04	27.69	23.95	19.16	16.50
	2.380	46.41	37.97	31.57	23.68	20.31	17.33	14.81
	2.968	39.83	32.84	27.82	20.95	17.33	15.46	12.82
	3.701	33.42	27.63	23.78	18.47	14.76	13.11	10.74

Table A4: Mean Spectral Velocity - Rock								
Portland Region Fault Model								
	Period	a	b	c	d	e	f	g
Mean	0.030	1.22	1.16	0.81	0.63	0.44	0.33	0.26
	0.045	2.15	2.09	1.47	1.14	0.78	0.58	0.45
	0.056	3.08	2.97	2.10	1.60	1.11	0.82	0.64
	0.069	4.43	4.23	2.99	2.27	1.58	1.16	0.91
	0.087	6.38	6.05	4.26	3.26	2.26	1.68	1.30
	0.108	9.30	8.75	6.10	4.72	3.24	2.44	1.88
	0.135	13.40	12.51	8.65	6.76	4.60	3.49	2.67
	0.168	18.33	16.94	11.72	9.23	6.23	4.71	3.61
	0.210	23.58	21.43	15.02	11.83	8.01	5.99	4.57
	0.261	28.86	25.65	18.29	14.45	9.87	7.32	5.54
	0.326	33.03	28.95	20.93	16.62	11.47	8.48	6.40
	0.407	34.63	30.52	22.27	17.67	12.36	9.14	6.92
	0.507	35.06	31.37	23.13	18.21	13.05	9.61	7.30
	0.632	36.55	32.96	24.79	19.30	14.36	10.44	8.06
	0.789	39.07	34.78	27.02	20.78	15.97	11.41	9.07
	0.984	41.43	35.69	28.57	21.91	16.97	12.04	9.80
	1.227	43.53	36.32	29.60	22.78	17.49	12.58	10.29
	1.530	44.21	36.37	29.72	22.87	17.49	13.01	10.59
	1.908	40.32	33.67	26.74	20.62	15.89	12.30	10.09
	2.380	34.10	29.33	22.06	17.19	13.39	10.57	8.89
	2.968	29.36	25.43	18.42	14.52	11.31	8.89	7.70
	3.701	22.79	19.26	13.95	11.06	8.52	6.67	5.85
84th	0.030	2.44	2.21	1.53	1.19	0.83	0.64	0.51
perc	0.045	4.31	3.95	2.80	2.32	1.50	1.16	0.86
	0.056	6.28	5.75	4.09	3.34	2.18	1.67	1.25
	0.069	9.13	8.33	5.93	4.82	3.16	2.42	1.83
	0.087	13.30	12.06	8.53	7.00	4.58	3.53	2.65
	0.108	19.48	17.53	12.25	10.20	6.60	5.16	3.85
	0.135	27.69	24.63	17.12	14.43	9.20	7.26	5.40
	0.168	36.62	32.08	22.37	19.04	11.99	9.46	7.04
	0.210	45.94	39.58	27.85	23.82	14.98	11.72	8.69
	0.261	56.19	47.40	33.84	28.93	18.37	14.26	10.48
	0.326	64.88	53.82	38.90	33.17	21.39	16.49	12.09
	0.407	67.68	56.05	40.78	34.52	22.66	17.37	12.86
	0.507	66.28	55.30	40.33	33.76	22.79	17.25	13.04
	0.632	65.73	54.67	40.30	33.43	23.48	17.43	13.66
	0.789	68.12	55.38	41.99	34.59	25.14	18.13	14.91
	0.984	73.31	57.74	45.13	36.63	27.13	19.19	16.34
	1.227	80.93	62.26	49.39	38.96	29.27	20.80	17.88
	1.530	86.11	66.41	52.29	39.90	30.54	22.44	19.26
	1.908	79.64	63.96	48.56	36.63	28.31	21.91	18.84
	2.380	65.44	55.66	40.19	30.58	23.57	19.02	16.47
	2.968	54.94	47.95	33.68	26.15	19.89	16.24	14.17
	3.701	46.37	39.60	28.03	22.19	16.70	13.55	11.85

FIGURE CAPTIONS

Figure 1. Schematic diagram of the strong ground motion simulation procedure. The fault surface is divided into discrete fault segments. The contribution from each segment is summed as described in the text to simulate rupture propagation across the fault surface.

Figure 2. Schematic diagram illustrating random component of rupture velocity *(top)* and slip time function *(bottom)*. The rupture onset time t_o for each fault segment is a random number having a Gaussian distribution centered between the arrival t_a and departure t_b times of the rupture front. The initiation t_{si} for each of the *nsrc* source functions is a random number having a Gaussian distribution centered on evenly spaced intervals of the source function's rise time T_e.

Figure 3. Comparison of recorded and simulated three-component time histories of the 1985 Michoacan earthquake at rock sites Caleta de Campos, La Villita, La Union, Zihuatanejo and Papanoa. Peak accelerations are in g, gravity, and time is in seconds.

Figure 4. Comparison of recorded and simulated 5% damped acceleration response spectra (in g, gravity) for: (a) five rock sites in coastal Mexico using the Cal, Mexico source function; (b) the Valparaiso U.F.S.M. rock site using the Valu, Chile source function; (c) five soil sites in Chile using the Vina, Chile source function.

Figure 5. Estimates of standard error (natural logarithm of spectral acceleration) in the simulation procedure associated with the three empirical source functions: Vina (Chile, soil site); Cal (Mexico, rock site); and Valu (Chile, rock site), Valu (Chile, rock site); and Cal (Mexico, rock site).

Figure 6. Source and station geometry for two separate hypothetical magnitude 8 subduction earthquakes in the Pacific Northwest. (a) map view, showing fault planes and fault segments (rectangular grids) and station array (open squares) for western Washington (dip=11) and Oregon (dip=21) fault models. Stations equidistant from the fault are grouped in lines, labeled a through g in the figure. Assumed depths to the plate interface are given in kilometers. (b) schematic cross-section through the center of the western Washington model showing rupture zone extent and simplified velocity structure; superimposed are the rupture zones of the Michoacan and Valparaiso earthquakes. The velocity structure used to generate Green's functions (see text) is modified from Taber and Lewis (1986). Depth and distance are in kilometers, with no vertical exaggeration, and velocities are in kilometers/second. The approximate locations of the 1949 Olympia (54 km depth) and 1965 Seattle (60 km depth) Wadati-Benioff zone earthquakes are indicated by stars.

Figure 7. Velocity structure of the Cascadia subduction zone (adapted from Spence *et al.*, 1985) used in finite-difference modeling for the three source locations shown by stars (18, 27, and 36 kilometers depth). Receiver locations are indicated by inverted triangles. Scale is in kilometers, with no vertical exaggeration. P and S wave velocities are in kilometers/second.

Figure 8. Comparison between 2-D finite difference (a-c) and 1-D ray theory (d-f) computed accelerations for the 15 receiver locations and the three sources shown in figure 7; the source depths are 18 (a,d), 27 (b,e), and 36 (c,f) kilometers, respectively. The finite difference results are for the velocity structure shown in figure 7, and the ray theory results are for the simplified velocity structure shown in figure 6b. There is an abrupt increase in the Moho reflected S amplitude as the wave field becomes post-critical. Time is in seconds, distance is in kilometers, and amplitude is unscaled acceleration.

Figure 9. Horizontal accelerograms for the three (shallow, middle, deep) distributions of slip in the western Washington fault model using a rock-site source function. Because of the close proximity of the receivers relative to the maximum slip of the asperities, the traces shown represent maximum ground motion amplitudes. Time is in seconds, and acceleration in g, gravity.

Figure 10. Horizontal accelerograms for the three (shallow, middle, deep) distributions of slip in the Oregon fault model. The traces shown represent maximum rock-site ground motion amplitudes. Time is in seconds, and acceleration is in g, gravity.

Figure 11. Horizontal PGA attenuation relations using two different distance measurements. (a) PGA vs. closest distance to the fault plane. (b) PGA vs. distance to nearest asperity. Distances are in kilometers, and peak acceleration is in g, gravity.

Figure 12. Average horizontal peak acceleration for each receiver location for three depth distributions of slip on the Oregon fault plane. The widest range of peak accelerations is produced when slip is concentrated in the top third of the fault plane (a), and the deep slip distribution (c) produces more uniform amplitudes. Peak accelerations are plotted on a common scale.

Figure 13. Comparison of horizontal PGA attenuation relations derived in this study with relations derived for rock sites *(left)* by Youngs *et al.* (1988) and for soil sites *(right)* by WPPSS (1988). The Youngs *et al.* (1988) relations are the same except for a soil amplification coefficient. The simulated PGA for different distances are shown as open symbols. The open circles are from the western Washington model and the open diamonds are from the Oregon fault model. The standard deviation of the mean is less than 5%, and the standard deviation of each population is shown by the vertical bars. Distances to the fault are in kilometers and PGA is in units of g, gravity.

Figure 14. Median and 84th percentile pseudo-velocity response spectra (5% damping) for the western Washington and Oregon fault models for each of the lines of stations shown in figure 6a. Plotted as velocity in centimeters/second vs. period in seconds.

Figure 15. (a) Comparison of simulated horizontal response spectra on soil in Seattle (line f) for three slip models (shallow asperity, deep asperity, and the log mean of the shallow, middle, and deep results) of a magnitude 8 earthquake with and empirical estimate from Crouse *et al.* (1988), and two estimates *for different distances from* Heaton and Hartzell (H&H) (1989). The empirical estimates are derived from global sets of recorded strong motion data. (b) Comparison of simulated horizontal response spectra on soil for the Seattle - Olympia region from a magnitude 8 subduction earthquake with the mean of 10 horizontal components recorded in Seattle, Tacoma and Olympia during the 1949 and 1965 Wadati-Benioff zone earthquakes. Pseudo-spectral velocity is in units of centimeters/second and is plotted against period in seconds.

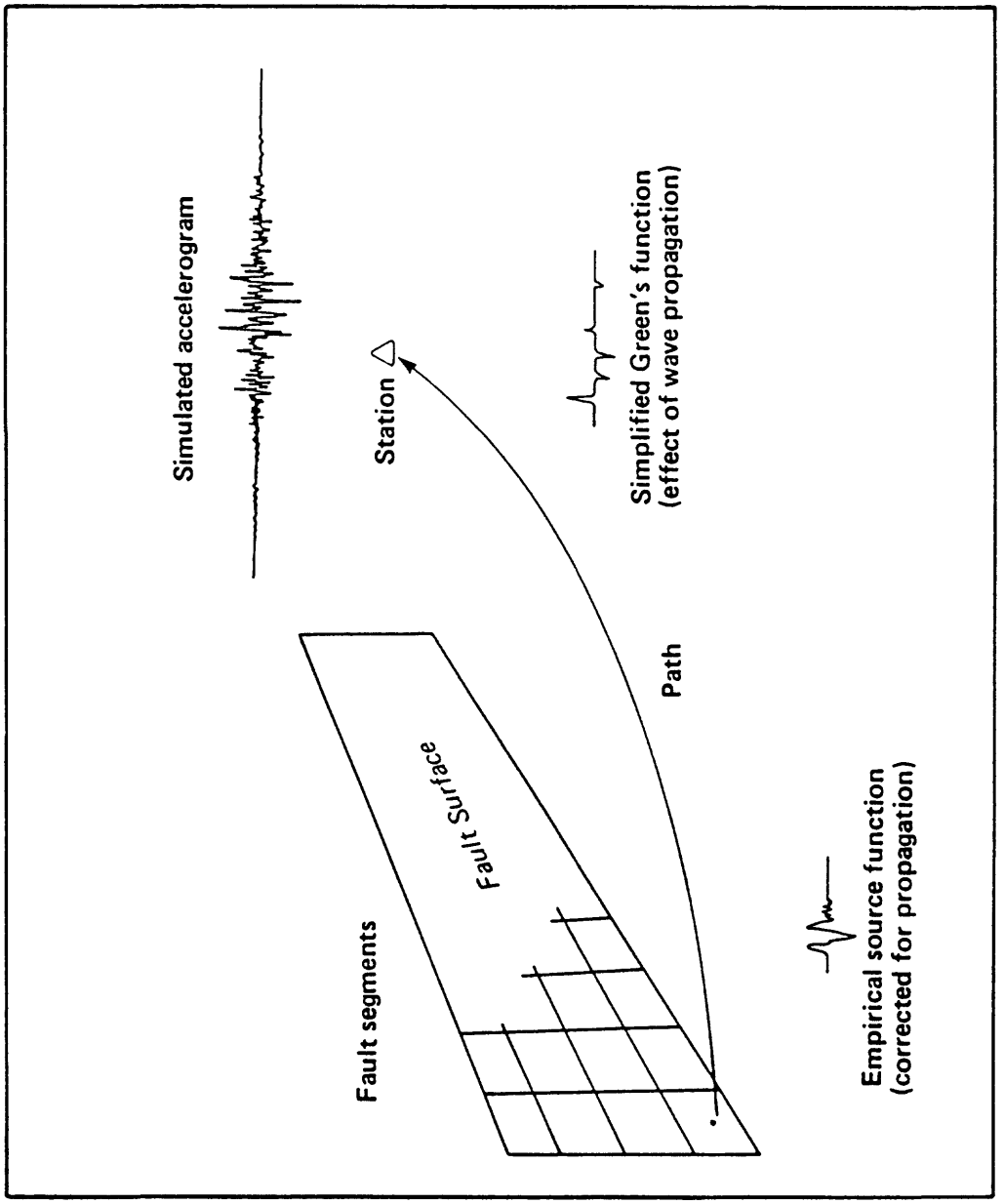
Simulated accelerogram
Station
Simplified Green's function
(effect of wave propagation)
Path
Fault Surface
Fault segments
Empirical source function
(corrected for propagation)

Figure 1

Rupture Velocity

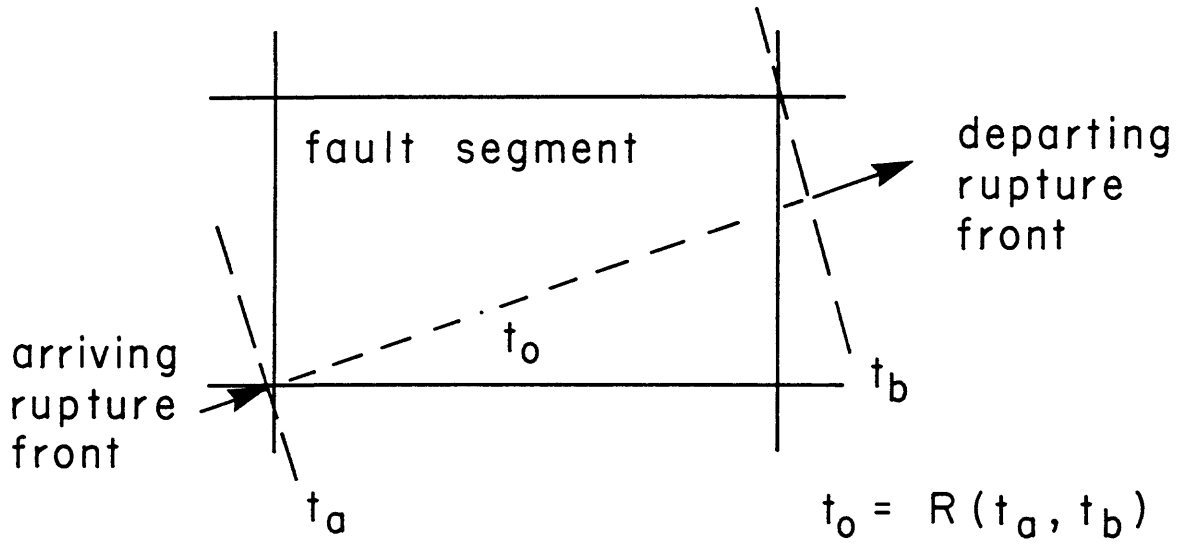

$$t_o = R(t_a, t_b)$$

Slip Time Function

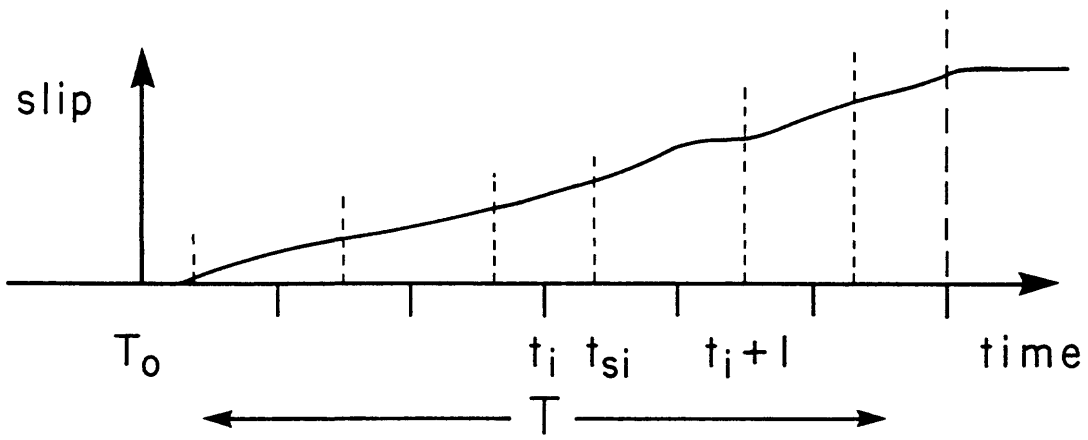

$$t_i = T_o + (i-1)\,Te$$

$$t_{si} = R(t_i, t_{i+1})$$

$$(i = 1,\ nsrc)$$

Figure 2

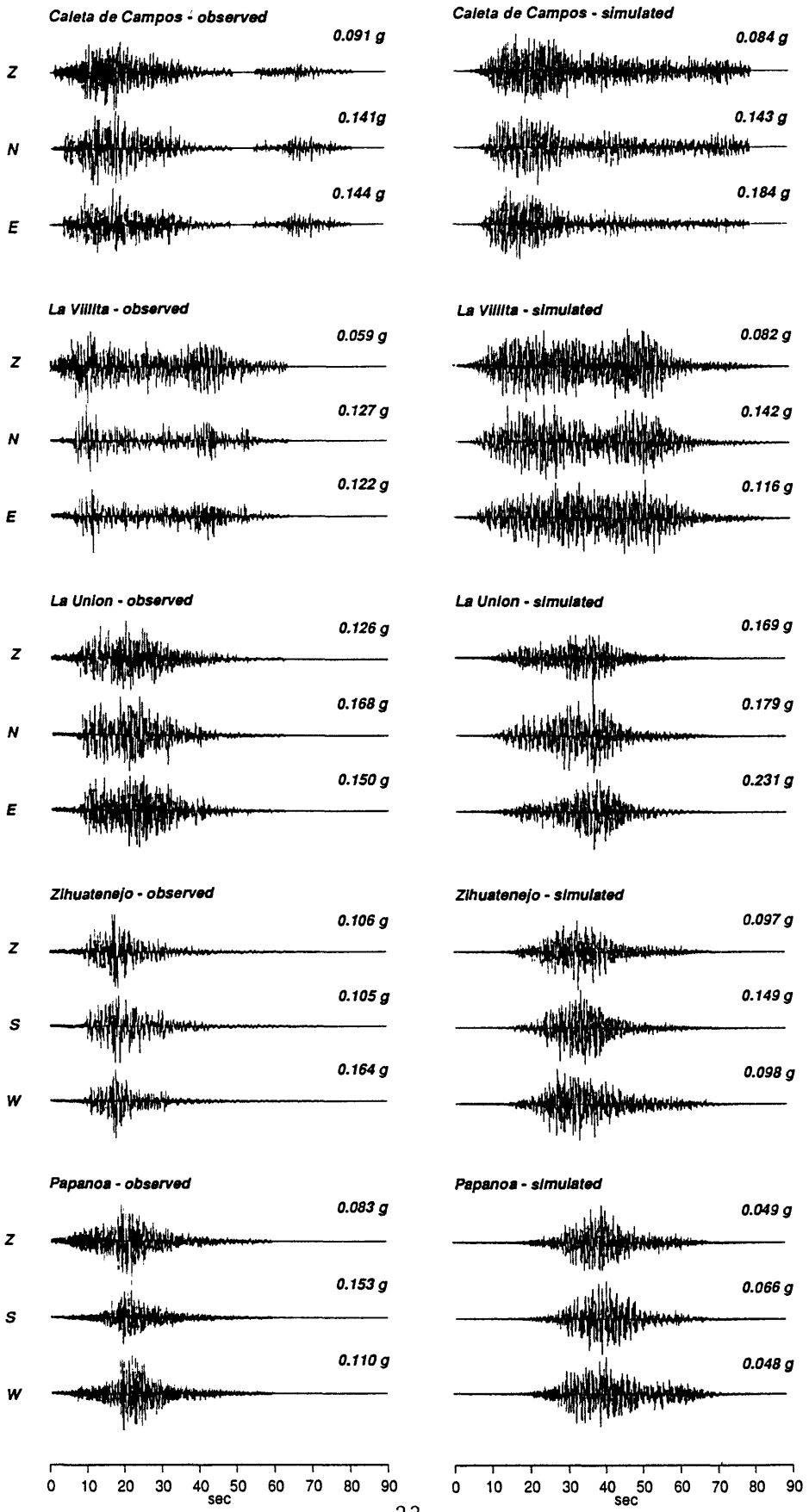
Michoacan Earthquake, 19 Sept 85
Caleta de Campos - observed
0.091 g
Z
0.141g
N
0.144 g
E
Caleta de Campos - simulated
0.084 g
0.143 g
0.184 g
La Villita - observed
0.059 g
Z
0.127 g
N
0.122 g
E
La Villita - simulated
0.082 g
0.142 g
0.116 g
La Union - observed
0.126 g
Z
0.168 g
N
0.150 g
E
La Union - simulated
0.169 g
0.179 g
0.231 g
Zihuatenejo - observed
0.106 g
Z
0.105 g
S
0.164 g
W
Zihuatenejo - simulated
0.097 g
0.149 g
0.098 g
Papanoa - observed
0.083 g
Z
0.153 g
S
0.110 g
W
Papanoa - simulated
0.049 g
0.066 g
0.048 g
0 10 20 30 40 50 60 70 80 90
sec
0 10 20 30 40 50 60 70 80 90
sec

Figure 3

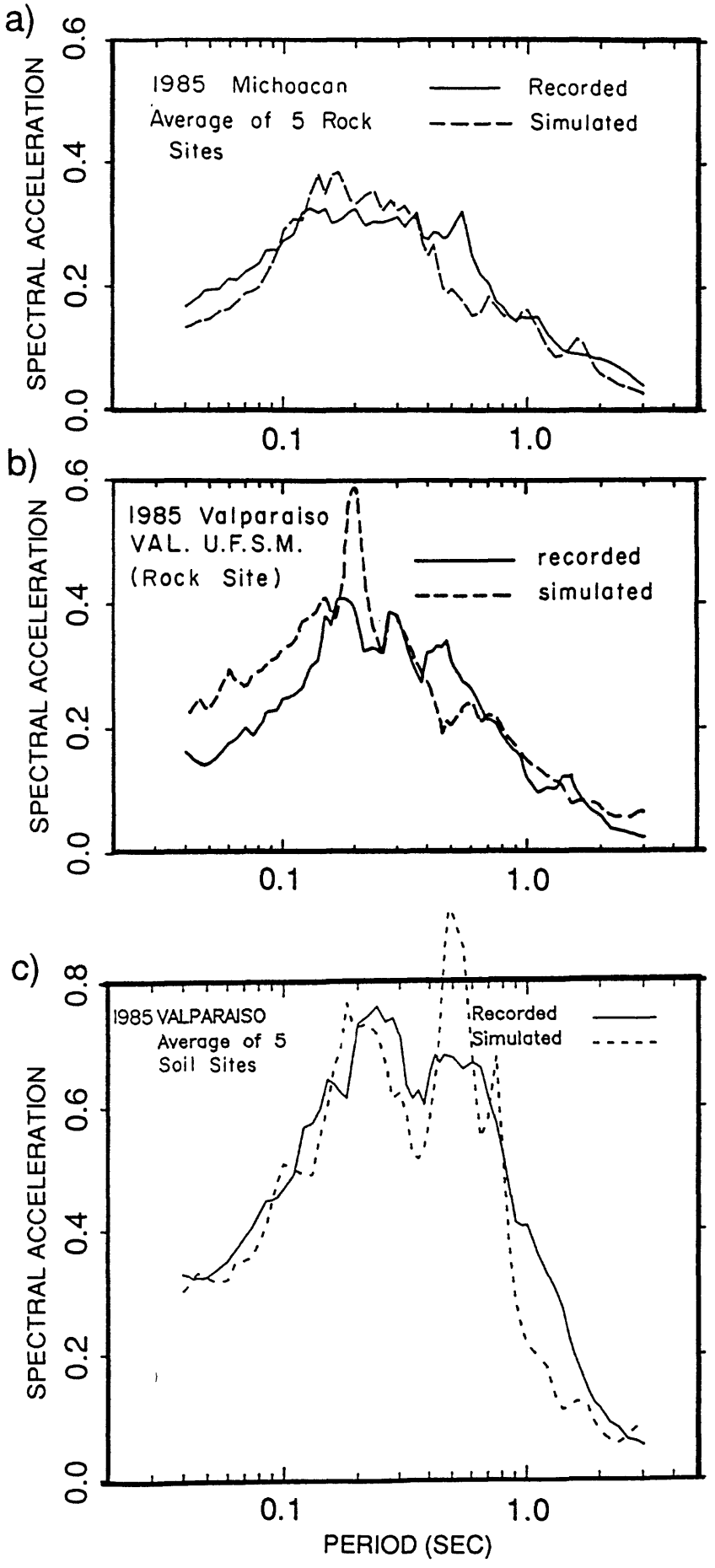
a)
1985 Michoacan
Average of 5 Rock
Sites
Recorded
Simulated
SPECTRAL ACCELERATION
0.0
0.2
0.4
0.6
0.1
1.0
b)
1985 Valparaiso
VAL. U.F.S.M.
(Rock Site)
recorded
simulated
SPECTRAL ACCELERATION
0.0
0.2
0.4
0.6
0.1
1.0
c)
1985 VALPARAISO
Average of 5
Soil Sites
Recorded
Simulated
SPECTRAL ACCELERATION
0.0
0.2
0.4
0.6
0.8
0.1
1.0
PERIOD (SEC)

Figure 4

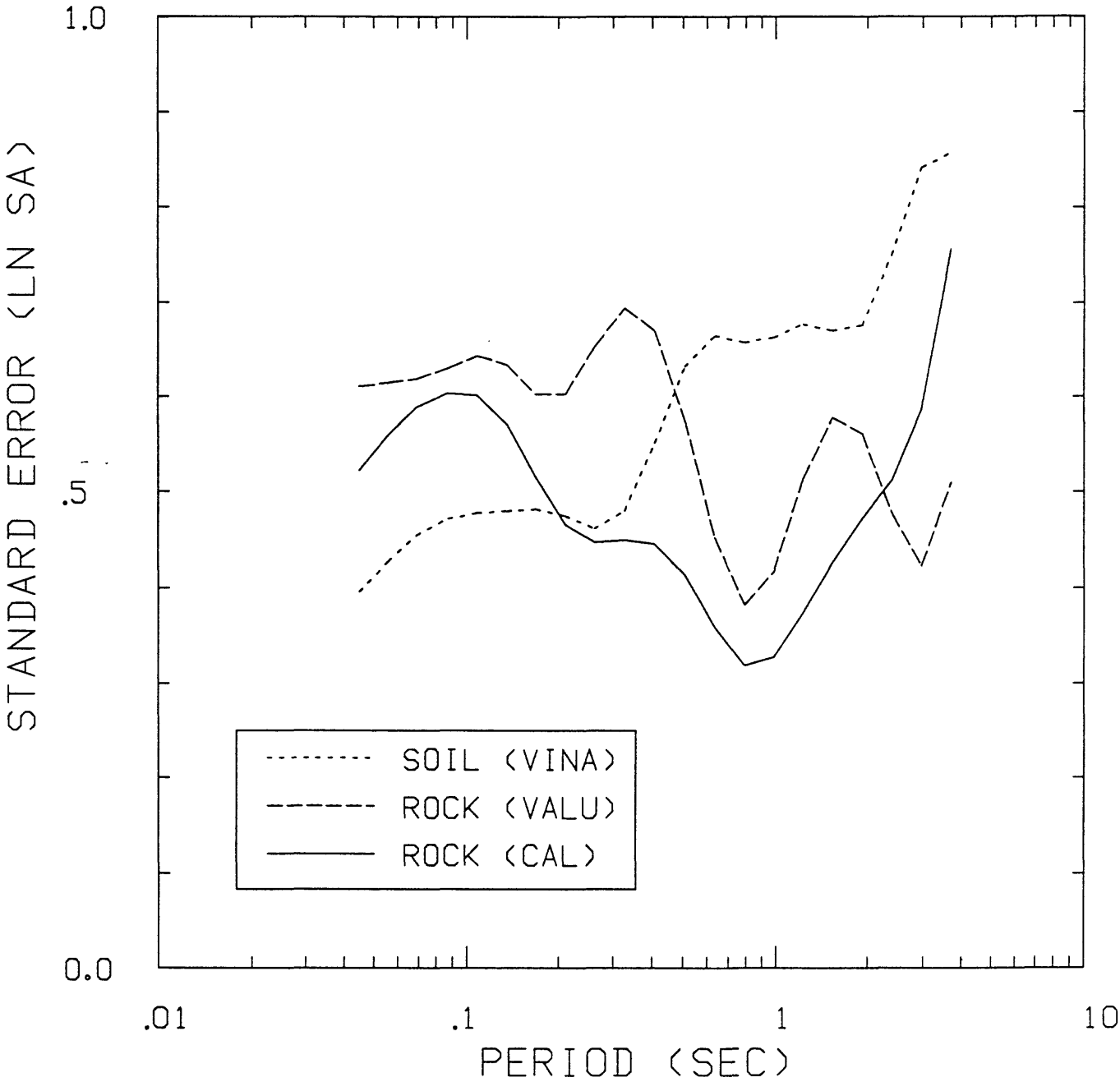
1.0
.5
0.0
STANDARD ERROR (LN SA)
.01
.1
1
10
PERIOD (SEC)
SOIL (VINA)
ROCK (VALU)
ROCK (CAL)

Figure 5

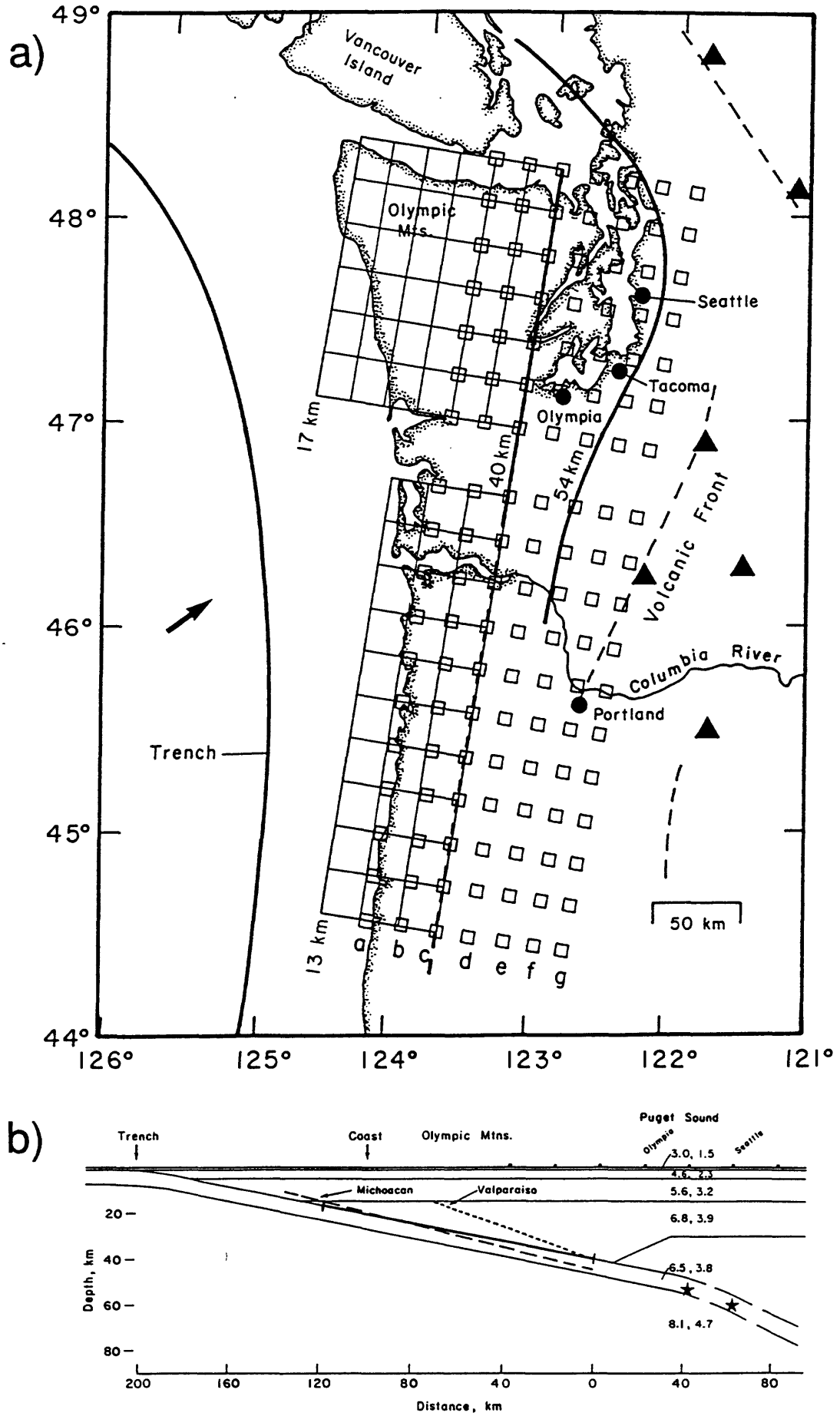
a)
49°
48°
47°
46°
45°
44°
126°
125°
124°
123°
122°
121°
Vancouver Island
Olympic Mts.
Seattle
Tacoma
Olympia
17 km
40 km
54 km
Volcanic Front
Columbia River
Portland
Trench
50 km
13 km
a b c d e f g
b)
Trench
Coast
Olympic Mtns.
Puget Sound
Olympia
Seattle
3.0, 1.5
4.6, 2.3
5.6, 3.2
6.8, 3.9
6.5, 3.8
8.1, 4.7
Michoacan
Valparaiso
Depth, km
20
40
60
80
200
160
120
80
40
0
40
80
Distance, km

Figure 6

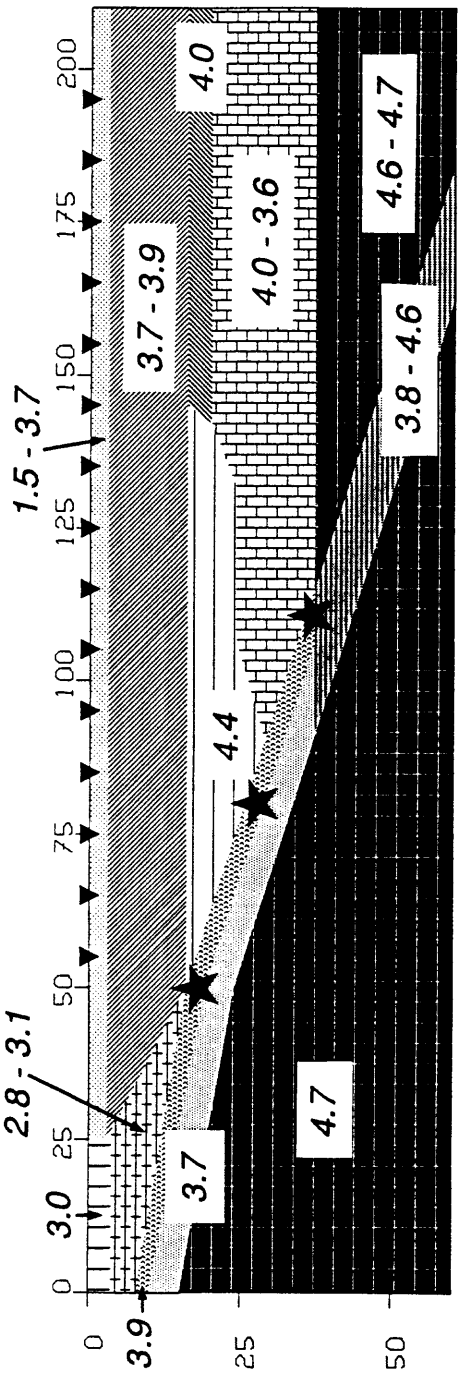
0
25
50
75
100
125
150
175
200
0
25
50
3.9
3.0
2.8 - 3.1
1.5 - 3.7
3.7
3.7 - 3.9
4.0
4.0 - 3.6
4.4
4.7
3.8 - 4.6
4.6 - 4.7

Figure 7

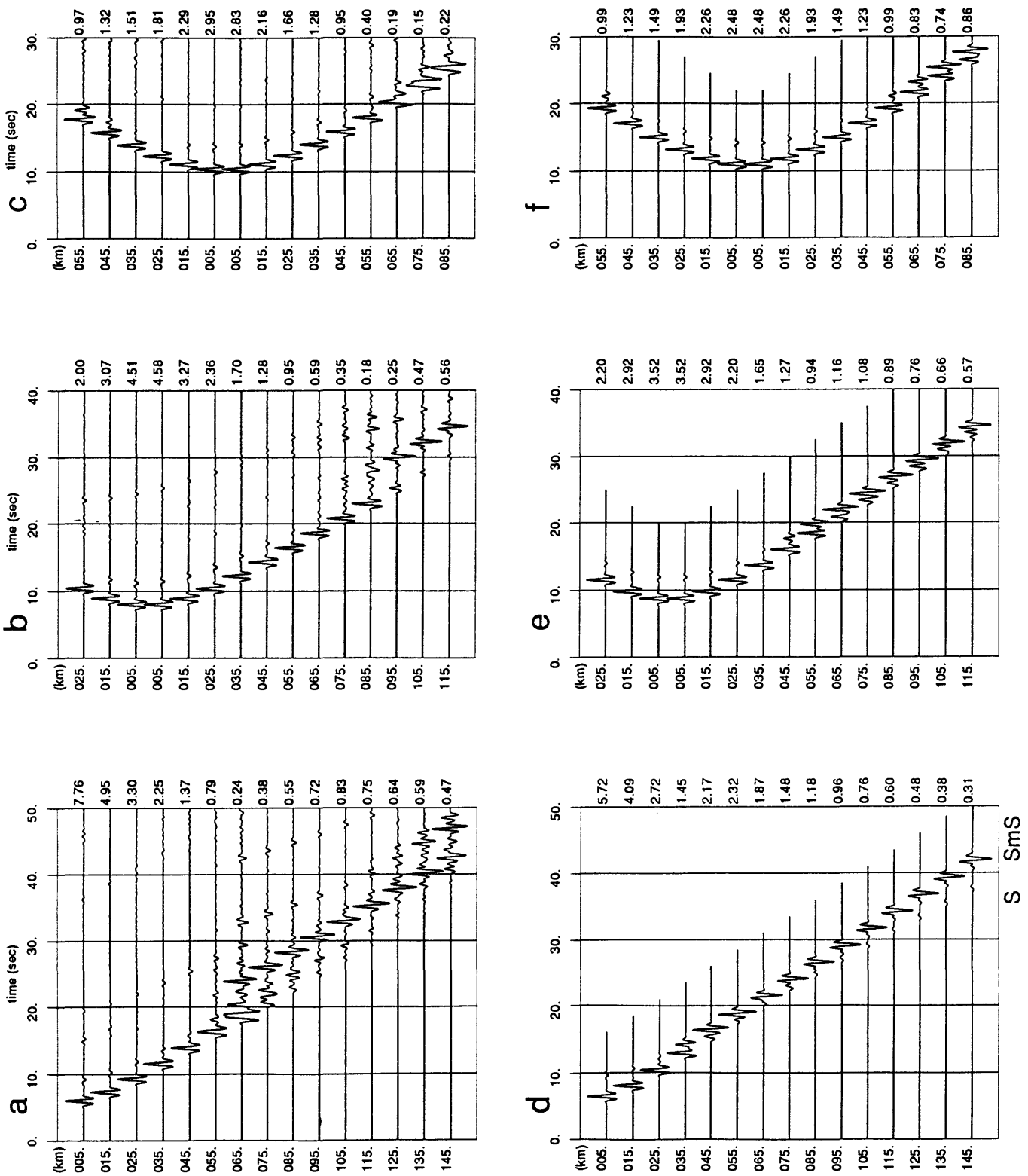

Figure 8

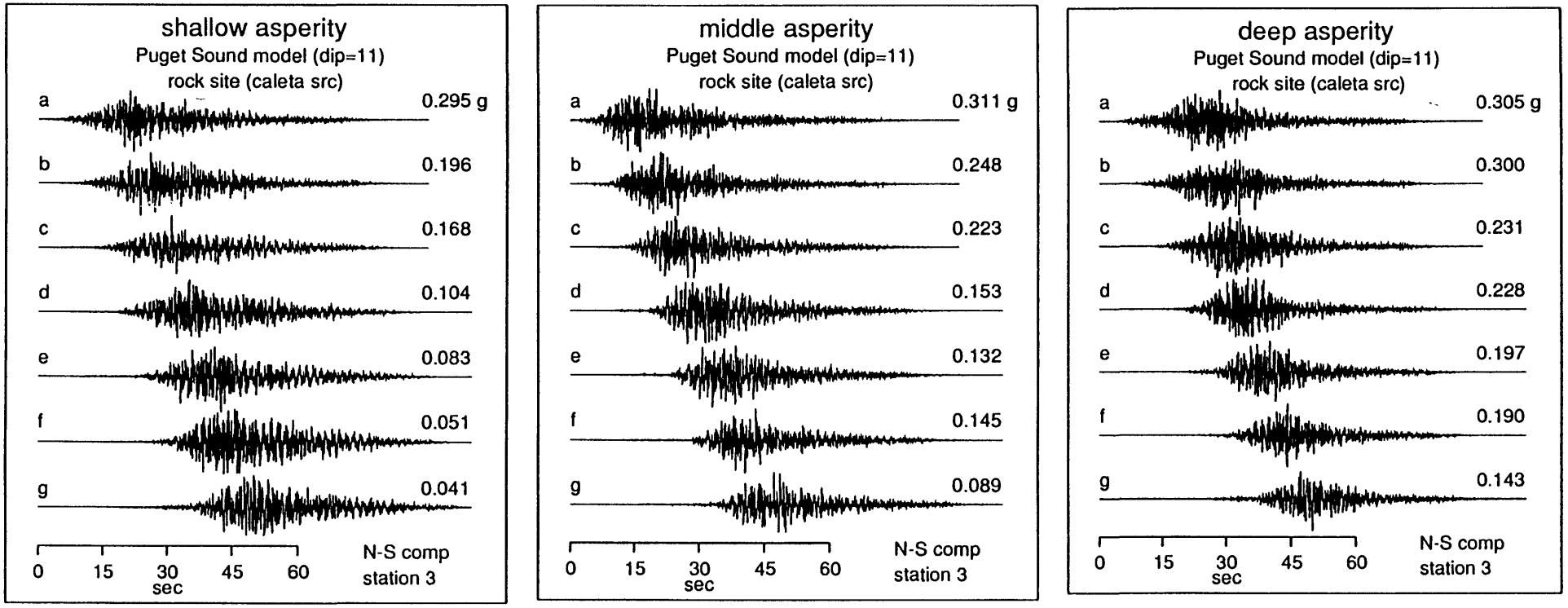
shallow asperity
Puget Sound model (dip=11)
rock site (caleta src)
a
0.295 g
b
0.196
c
0.168
d
0.104
e
0.083
f
0.051
g
0.041
0
15
30
45
60
sec
N-S comp
station 3
middle asperity
Puget Sound model (dip=11)
rock site (caleta src)
a
0.311 g
b
0.248
c
0.223
d
0.153
e
0.132
f
0.145
g
0.089
0
15
30
45
60
sec
N-S comp
station 3
deep asperity
Puget Sound model (dip=11)
rock site (caleta src)
a
0.305 g
b
0.300
c
0.231
d
0.228
e
0.197
f
0.190
g
0.143
0
15
30
45
60
sec
N-S comp
station 3

Figure 9

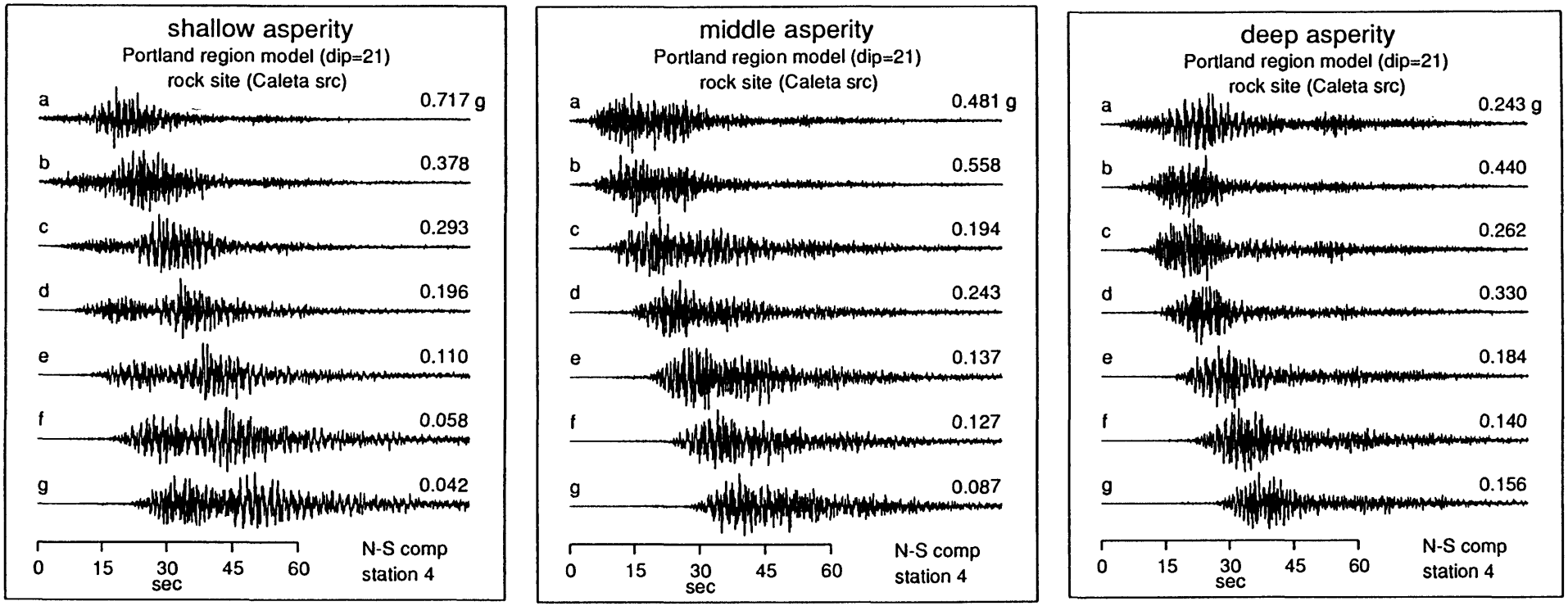
shallow asperity
Portland region model (dip=21)
rock site (Caleta src)
a 0.717 g
b 0.378
c 0.293
d 0.196
e 0.110
f 0.058
g 0.042
0 15 30 45 60
sec
N-S comp
station 4
middle asperity
Portland region model (dip=21)
rock site (Caleta src)
a 0.481 g
b 0.558
c 0.194
d 0.243
e 0.137
f 0.127
g 0.087
0 15 30 45 60
sec
N-S comp
station 4
deep asperity
Portland region model (dip=21)
rock site (Caleta src)
a 0.243 g
b 0.440
c 0.262
d 0.330
e 0.184
f 0.140
g 0.156
0 15 30 45 60
sec
N-S comp
station 4

Figure 10

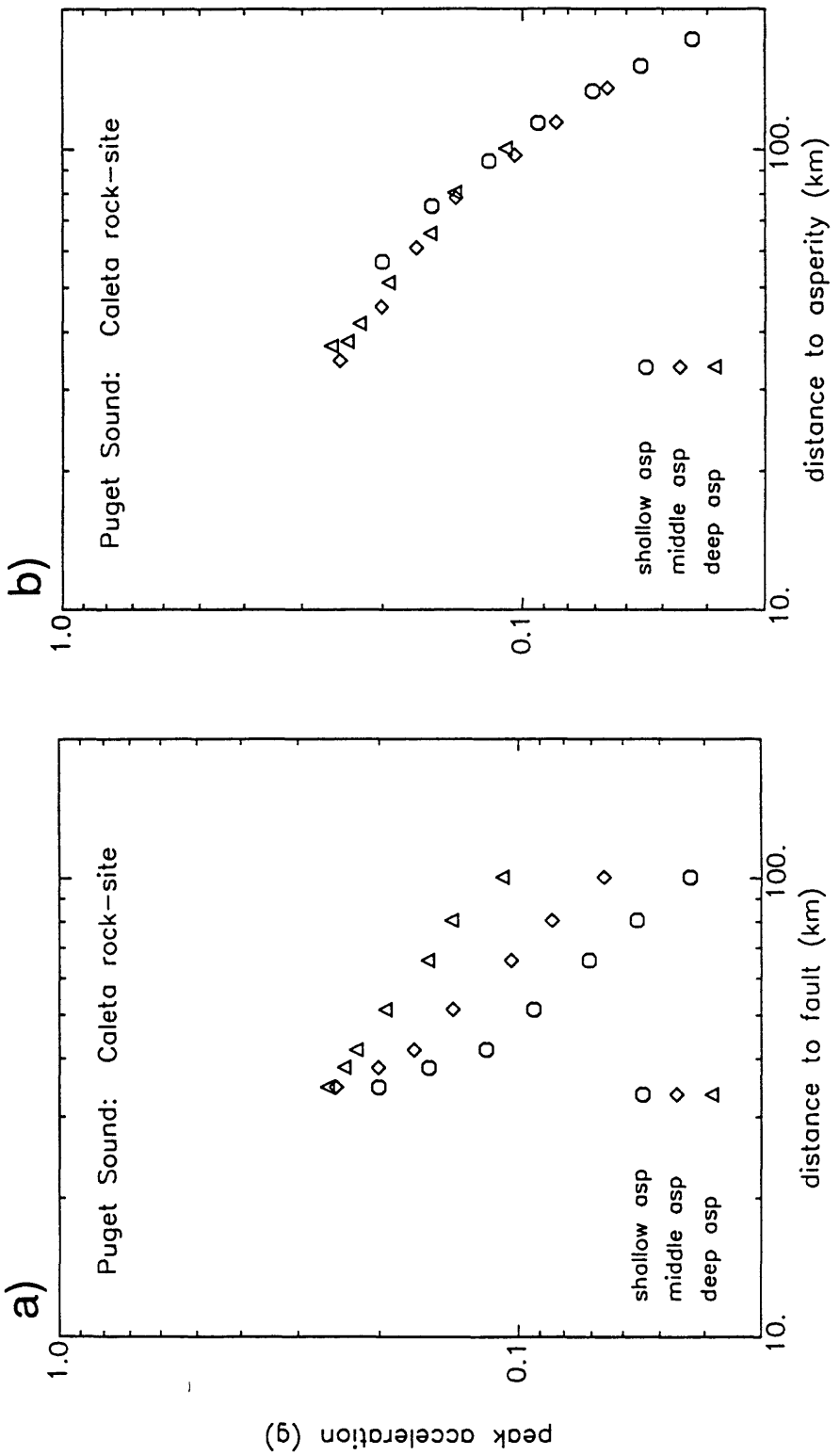
a)
Puget Sound: Caleta rock-site
shallow asp
middle asp
deep asp
peak acceleration (g)
1.0
0.1
10.
100.
distance to fault (km)
b)
Puget Sound: Caleta rock-site
shallow asp
middle asp
deep asp
1.0
0.1
10.
100.
distance to asperity (km)

Figure 11

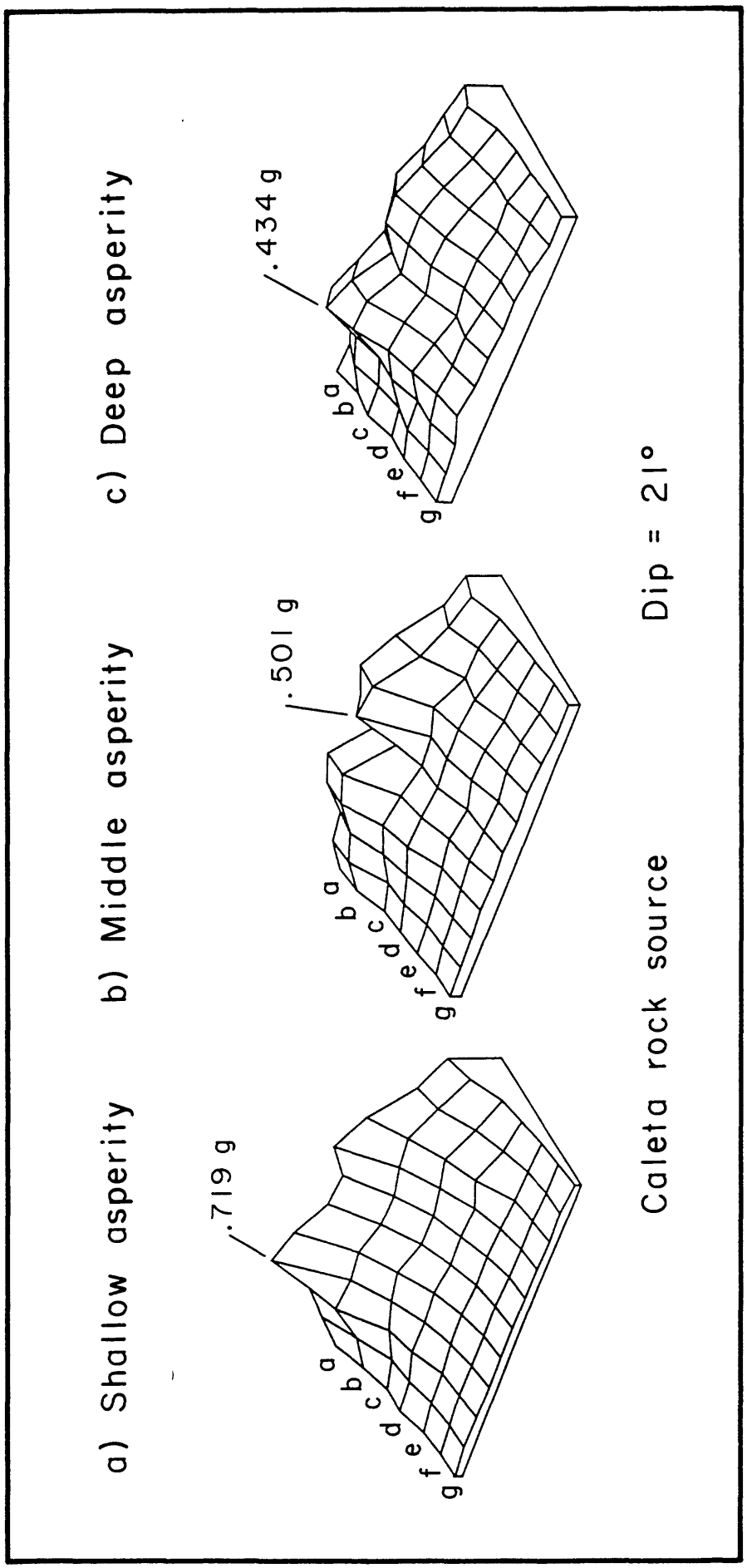
a) Shallow asperity
b) Middle asperity
c) Deep asperity
.719 g
.501 g
.434 g
a
b
c
d
e
f
g
Caleta rock source
Dip = 21°

Figure 12

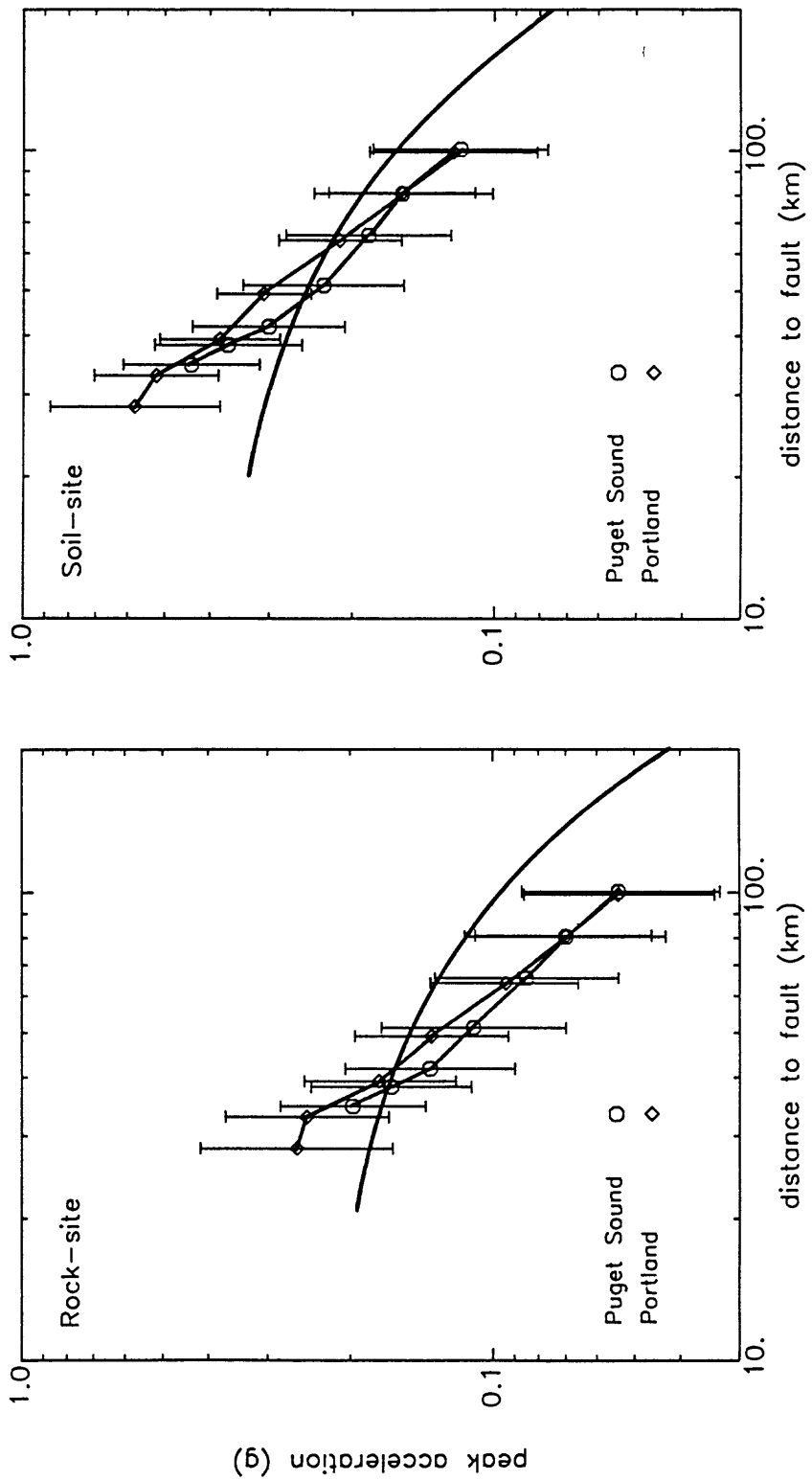
Soil-site
Rock-site
Puget Sound
Portland
peak acceleration (g)
distance to fault (km)
1.0
0.1
10.
100.

Figure 13

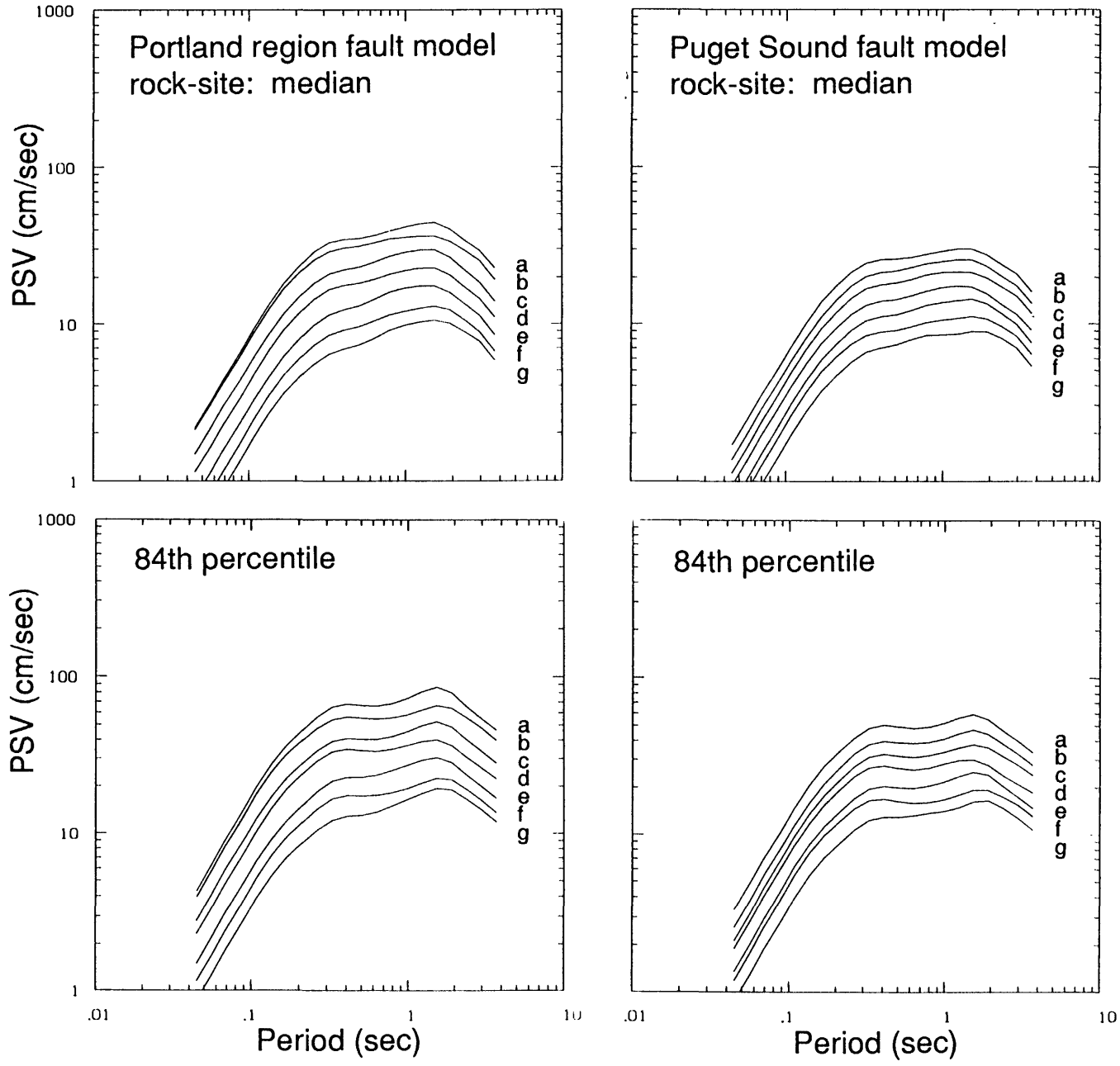
Portland region fault model
rock-site: median
Puget Sound fault model
rock-site: median
84th percentile
84th percentile
PSV (cm/sec)
PSV (cm/sec)
1000
100
10
1
.01
.1
1
10
Period (sec)
Period (sec)
a
b
c
d
e
f
g

Figure 14

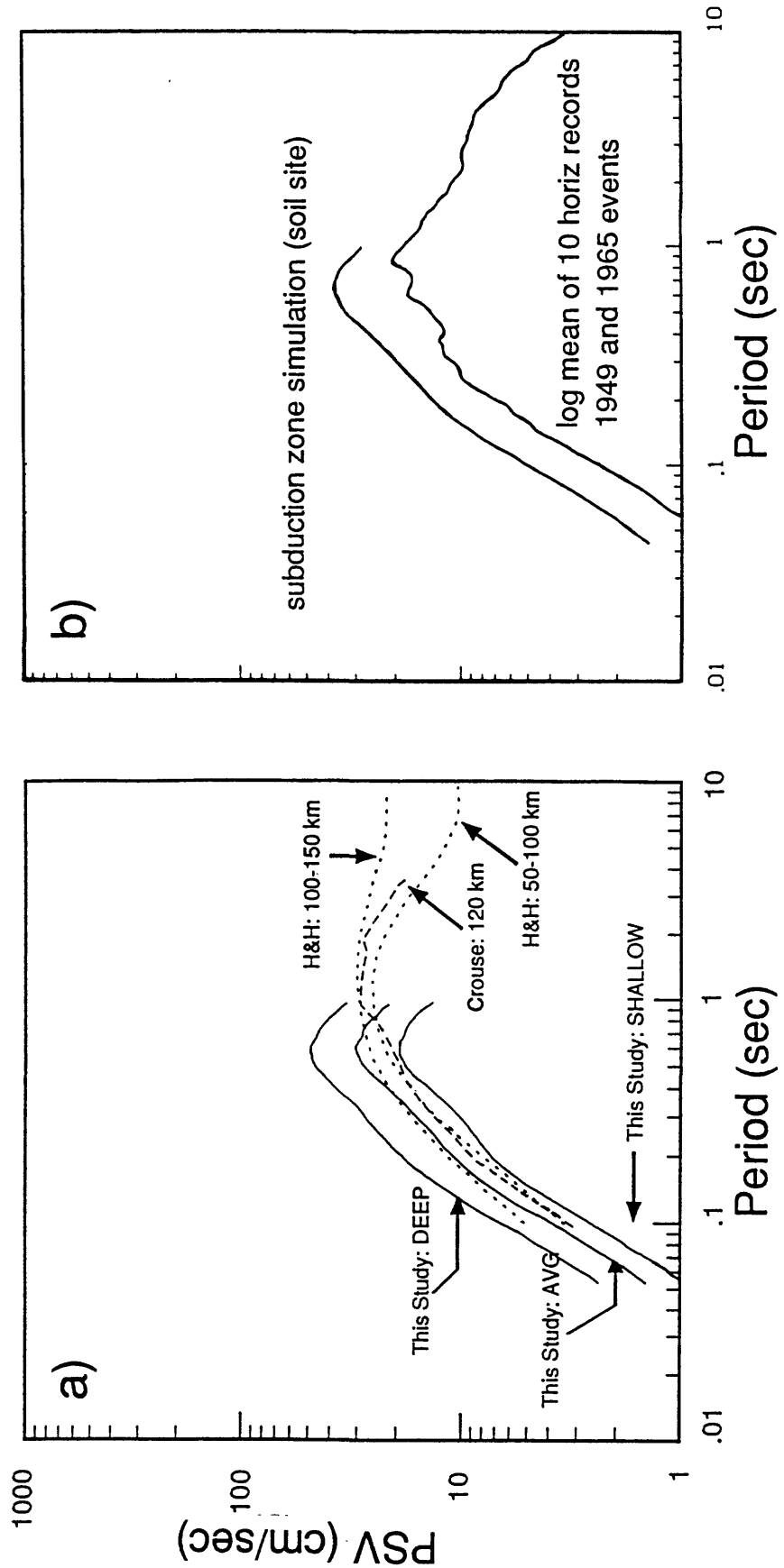
a)
PSV (cm/sec)
1000
100
10
1
.01
.1
1
10
Period (sec)
H&H: 100-150 km
Crouse: 120 km
H&H: 50-100 km
This Study: DEEP
This Study: AVG
This Study: SHALLOW
b)
subduction zone simulation (soil site)
log mean of 10 horiz records
1949 and 1965 events
.01
.1
1
10
Period (sec)

Figure 15